

FILE COPY
MS FILE COPY

Tectonophysics, 114 (1985) 55-102
Elsevier Science Publishers B.V., Amsterdam - Printed in The Netherlands

55

①
AD-A196 424

INVERSION OF REFRACTION DATA FROM THE FRAM AND NANSEN BASINS OF THE ARCTIC OCEAN

GREGORY L. DUCKWORTH ¹ and ARTHUR B. BAGGEROER ²

¹Department of Earth, Atmospheric, and Planetary Sciences, Rm E34-458, Massachusetts Institute of Technology, Cambridge, MA 02139 (U.S.A.)

²Departments of Ocean and Electrical Engineering, Rm 5-204, Massachusetts Institute of Technology, Cambridge, MA 02139 (U.S.A.)

(Received by September 7, 1984; accepted September 25, 1984)

ABSTRACT

Duckworth, G.L. and Baggeroer, A.B., 1985. Inversion of refraction data from the Fram and Nansen Basins of the Arctic Ocean. In: E.S. Husebye, G.L. Johnson and Y. Kristoffersen (Editors). Geophysics of the Polar Regions. *Tectonophysics*, 114: 55-102.

As a part of the Fram 2 experiment (March-May 1980) six refraction lines were shot in the Pole Abyssal Plain or Fram Basin of the eastern Arctic Ocean. During the Fram 4 experiment (March-May 1982), four refraction lines were also shot in the Nansen basin just northeast of the Yermak Plateau. The Fram 2 lines at 86°N, 24°W cover both the abyssal plain region and the northern flank of the Morris Jessup Rise near magnetic anomalies 22 and 23. The Fram 4 lines near 83°N, 15°-20°E are on slightly younger crust at anomaly 12. In this paper we introduce new methods for processing and inversion of Arctic refraction data and contrast the results from these tectonically similar regions on opposite sides of the spreading center at the Arctic Mid-Ocean (Nansen) Ridge.

In both experiments the data were recorded digitally on a two-dimensional array of 24 hydrophones located 93 m below the floe camps. These multi-channel data are processed by high-resolution array processing techniques to yield velocity spectra over the short 1 km apertures of the arrays. These velocity spectra are transformed to tau-slowness and offset-slowness parameterizations and are inverted by (1) velocity-depth migration, (2) tau-sum, and (3) extremal inversion techniques to obtain crustal velocity models down to the Moho. Without the ability of the array processing to discern late breaking primaries, multiples, and shear arrivals, the sparsely shot lines with 5-15 offsets over the 30-100 km line lengths would not be invertible by these methods. These results demonstrate the effectiveness of arrays in determining crustal structure under the constraints of Arctic ice pack environment.

INTRODUCTION

The Fram 2 and Fram 4 ice camp experiments collected seismic reflection and refraction data in tectonically similar regions of the eastern Arctic Ocean basin (see Fig. 1). The camps were located on opposite sides of the spreading center at the

0040-1951/85/\$03.30 © 1985 Elsevier Science Publishers B.V.

DISTRIBUTION STATEMENT A

Approved for public release
Distribution Unlimited

88 6 6 011

Arctic Mid-Ocean Ridge (Nansen Ridge) and covered crust of slightly different age. The Fram 2 experiment was staged in the Pole Abyssal Plain (Fram Basin) to the west of the ridge and was near the Morris Jessup Rise between magnetic anomalies 22 and 23 while the Fram 4 experiment was in the Nansen Basin to the east of the ridge, near the Yermak Plateau at anomaly 12. Although the experiments were not chronologically symmetric about the ridge axis, both are informative about the structures of the thickened crustal regions at the Morris Jessup Rise and Yermak Plateau. These features are hypothesized to have formed at the ridge primarily

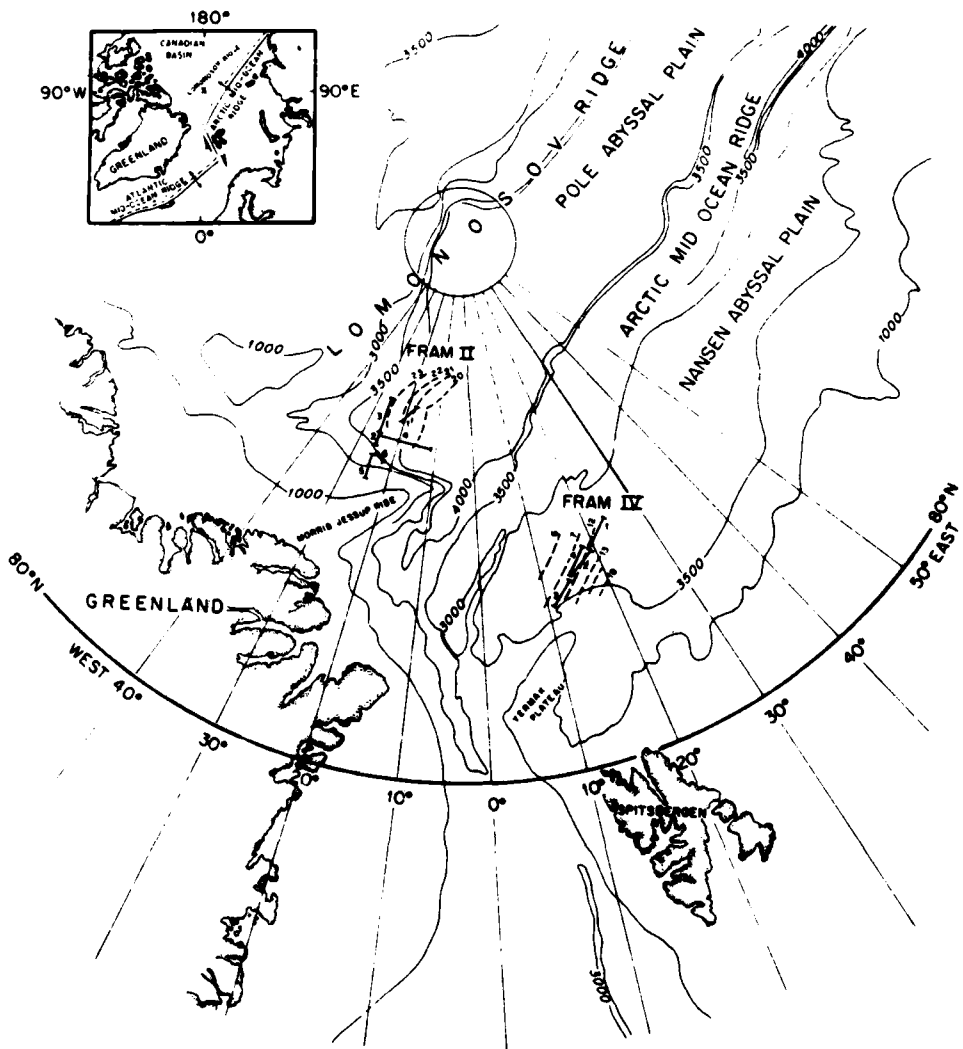


Fig. 1. Location and bathymetry of camps Fram 2 and Fram 4 in the Eastern Arctic Ocean. Also shown are the refraction lines (solid lines labeled 1-6) and the major magnetic anomalies in the areas studied (dashed lines). Inset: location of the spreading center at the Arctic Mid-Ocean Ridge.

between magnetic anomaly 13 and 18 time, and separated with the plate motion (Feden et al., 1979; Vogt et al., 1979; Jackson et al., 1984). The map of the Arctic in Fig. 1 shows the positions of the refraction lines, gross bathymetry, picked magnetic anomalies, the spreading center at the mid-ocean ridge, and the ice camps.

The continuous ice coverage at Fram 2 (nominally 86°N , 24°W) and Fram 4 (nominally 83°N , 17°E), required methods for data acquisition other than the popular methods for marine refraction work such as towed source/towed receiver, towed receiver array, and sonobuoy techniques. The procedure used for both experiments was to fix a 24 channel two-dimensional horizontal array of hydrophones with a 1 km aperture through the ice at the base camp. Explosive shots for the refraction lines were deployed by helicopter at various azimuths and offsets from the ice camps. Because the entire ice pack drifts with respect to the ocean floor, coverage of the areas shown in Figs. 2 and 3 was possible during the one month

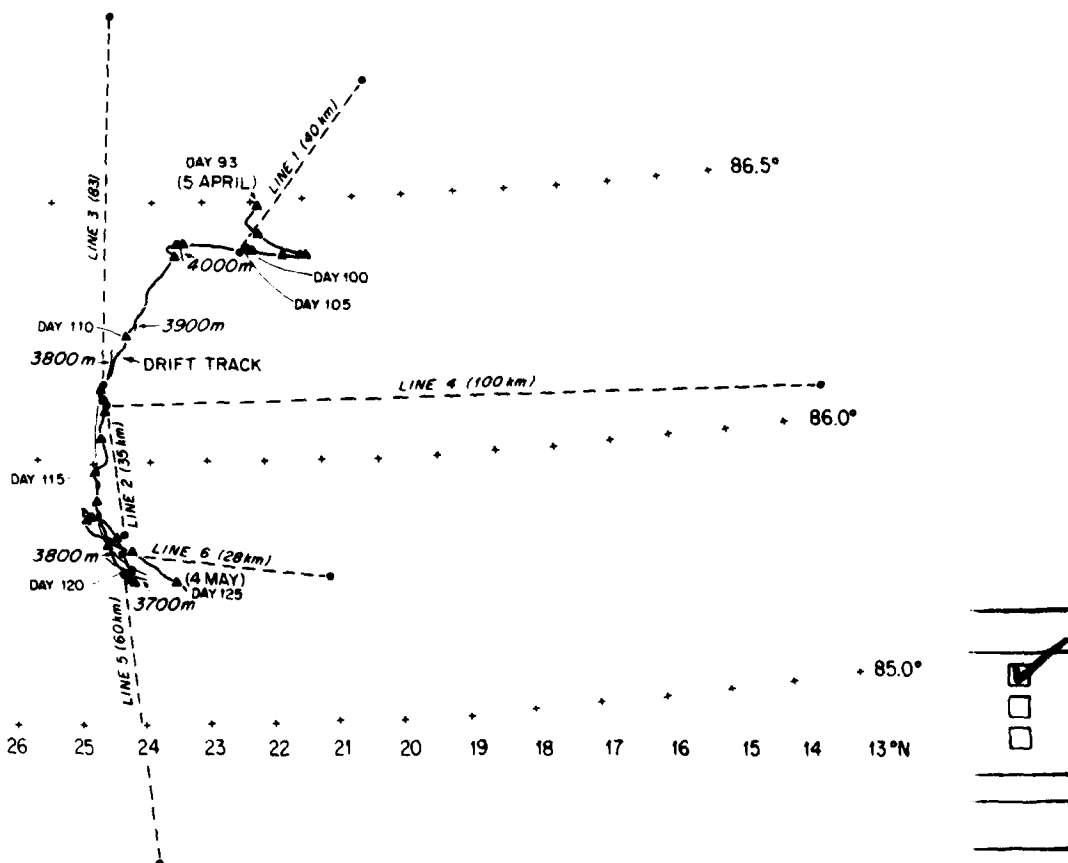
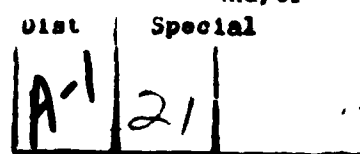


Fig. 2. The detailed drift track of camp Fram 2. The noon positions are denoted by triangles. Also indicated are water depths along the track and the refraction lines carried out during the experiment.



working life of each of the camps. Further detail on our methods for Arctic refraction can be found in Baggeroer and Falconer (1982) and Duckworth et al. (1982).

The reception of data on a multichannel array allows a slowness decomposition similar to the slant-stack to directly estimate the traveltimes, $t(p)$, offset $x(p)$, and delay time, $\tau(p)$, functions from the data. These functions are further decomposed by their instantaneous temporal frequency spectrum. To do this, decompositions are obtained from a velocity, or slowness, p , analysis algorithm utilizing a frequency domain adaptive array processing technique (Duckworth et al., 1982) adapted from the MLM technique (Capon et al., 1967). This method has the advantages of allowing high-resolution estimation of apparent slowness with the limited array aperture, and the rejection of aperture artifacts resulting from the use of a sparse and non-uniformly sampled two-dimensional array (Duckworth, 1983). This array structure was chosen to achieve good resolution and over a large frequency bandwidth without spatial aliasing. In addition, the 2-D coverage allows lines to be run at all azimuths from the camp. The control of the aperture artifacts afforded by the velocity spectral analysis technique allows late breaking multiples and shear arrivals

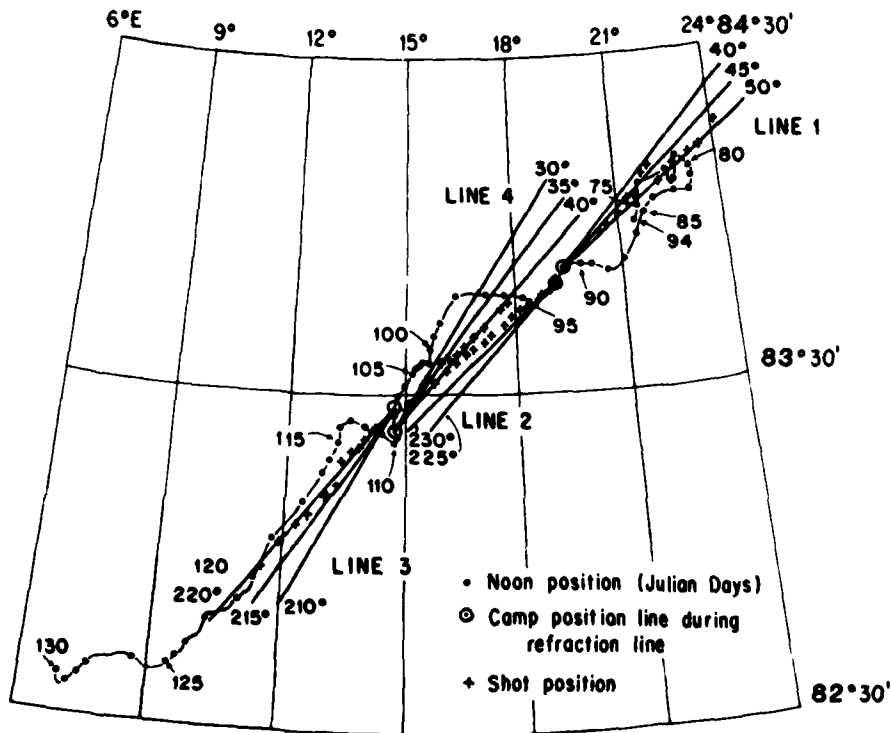


Fig. 3. The detailed drift track of camp Fram 4 and the refraction lines carried out during the experiment.

to be resolved in the coda, greatly enhancing the amount of usable data collected.

The results obtained in this paper indicate crustal structures in the Abyssal Plain regions which are slightly thinner than average. Other work has indicated that this might be a characteristic of slow spreading ridges, such as the Arctic Mid-Ocean Ridge (Jackson et al., 1982). We find that the crust thickens as the Yermak Plateau and Morris Jessup Rise are approached, yet it retains an oceanic structure on the lower flanks of these features. Rough basement topography disallows determination of shear velocities in the Nansen Basin (Fram 4); however, good coupling to shear at the basement interface does occur on some of the Fram 2 data, and a shear velocity structure which yields good estimates of the Poisson's ratio below basement is obtained.

Because this paper deals with the results from a large amount of data, only representative examples of the data and inversion procedure will be given. The first line on Fram 2 will be dealt with in some detail, and later lines will be treated only by typical model results and comments made only about their unique aspects.

NAVIGATION, SHOT POINT LOCATION, AND BATHYMETRY

The Fram 2 and Fram 4 camp positions were determined by satellite navigation using the U.S. Navy Transit Satellite network. Because the five satellites in the system are in polar orbits, a satellite was nearly always in view, and fixes were obtained approximately every hour. These raw data were then smoothed and interpolated by a Kalman filtering algorithm to yield densely sampled camp drift tracks shown in Figs. 2 and 3 (Allen et al., 1980; Tiemann et al., 1982). The sensor locations relative to a 200 m optical baseline were determined by standard surveying techniques. This yielded sensor "through-ice" positions * to within a meter near the vertex of the array, and within 5 m at the greatest extents of the array (about 600 m from the vertex). The absolute rotation of the baseline was determined by daily sun shots.

The offsets of the shot points were obtained by measurements of the traveltimes of the direct water arrival and ray tracing using water column sound velocity profiles measured by Expendable Sound Velocimeters (XSV). The ranging accuracy for this experiment is estimated to be ± 50 m. The bearing from the array to the shot was determined by azimuthal beamforming on the direct water arrival at the water wave

* We could obviously only survey the surface locations. Because of ocean currents relative to the floe, the actual sensor locations will deviate on a watch circle. It was assumed that the currents were of constant direction and magnitude over the 1 km aperture of the array and thus the relative locations measured at the surface were correct. The sensors used for this experiment employed a heavy 3 conductor shielded cable and a 1/4 inch polypropylene line supporting a two-mass compliant section for strum decoupling. The depth of the sensors was 300 ft (93 m) and the total suspended weight was 35 lbs. It is believed that all relative currents were less than 0.5 kt.

slowness. The details of the procedure are given by Duckworth (1983). The spectral characteristics of the shots are summarized in Duckworth et al. (1982).

A 12 kHz echo sounder was used to determine the bathymetry at the Fram 2 and Fram 4 camps from which the arrays were deployed. Good bathymetric control is important because dip can cause the measured slownesses and traveltimes to be erroneously interpreted. Further, evidence of rough topography can indicate that inversion for horizontally layered structures is inappropriate. The raw data from this system were processed and the uncorrected depths reported by Allen et al. (1980) for Fram 2, and Tiemann et al. (1982) for Fram 4. The raw data were corrected for our water column model by ray tracing at vertical incidence. To obtain the bathymetry at the source locations, the difference between direct arrival and the normal incidence reflection of the explosion signature from the bottom was used. It is felt that the accuracy of this method was sufficient to give bathymetry to within 20 m in regions of low relief. The Fram 2 experiment holds well to this assumption, however, there is evidence on the Fram 4 experiment that side-swipe may be present on some of the rougher lines.

THE FRAM 2 EXPERIMENT IN THE FRAM BASIN

Introduction

The Fram 2 experiment was carried out in the Pole Abyssal Plain, or Fram Basin, of the eastern Arctic Ocean from March to May of 1980. Figure 1 shows the locations of the refraction lines, bathymetry, and magnetic anomalies. In this work, lines 1, 4, and 6 will be discussed. Line 1 is in a deep region of the plain with almost no topographic relief and runs at 20° true between magnetic anomalies 21 and 22 corresponding to a crustal age of between 48–53 Ma (Ness et al., 1980). Line 4 runs approximately perpendicular to the magnetic lineations at 100° true, and is generally dipping away from the receiving array. The line spans the region from anomaly 23 to anomaly 20. It should be noted that this anomaly interpretation is subject to significant error because the clarity of the magnetic lineations deteriorates as the Morris Jessup Rise is approached. Finally, line 6 was carried out on the flanks of the Morris Jessup Rise as the camp shoaled late in the experiment. This line was shot along a non-negligible dip of 0.5° to 0.7° at approximately 104° true and shows little relief beyond this relatively constant dip. The magnetics in this region are very confused (Vogt et al., 1979).

The detailed drift track for the camp from April 5 until May 4, 1980 is shown in Fig. 2, along with the refraction lines and bathymetry. The details of the array and ice camp layout are given by Duckworth et al. (1982).

Fram 2 line 1

Experimental parameters

Line 1 of the Fram 2 experiment was carried out on April 12, 1980. At the start of

the run (1400Z), the camp was at 86.40°N and 22.20°W. At the end of the run (1900Z), the camp location was 86.40°N and 22.21°W. The distance between these endpoints is less than 0.1 km, so the camp may be regarded as stationary for the duration of the line.

For this line, the data acquisition system was not writing the master clock times correctly onto the data tapes, thus disabling the accurate offset determination. However, in parallel with our system, the Bedford Institute of Oceanography (BIO) was operating an ice tethered ocean bottom seismometer and an independent shot instant monitor. The surface offsets for the array data were obtained by correcting the offset determination of the BIO system for the offset between the BIO instrument and the array apex using an estimated tether angle. It is estimated that the offset errors using this method are bounded by 200 to 300 m. The offsets obtained were also checked using the travel time and slowness measurements for the direct water arrival and the first bottom bounce (refraction) assuming a sediment model as well as the water column profile. The formula for this offset is:

$$x = \frac{[(t_1 - t_2) - (\tau_1 - \tau_2)]}{(p_1 - p_2)}$$

where $\tau_1 = \tau(p_1)$ and $\tau_2 = \tau(p_2)$ from the model prediction, and (t_1, p_1) are the direct water wave coordinates and (t_2, p_2) are the bottom arrival coordinates observed on the velocity spectrum. The linear slowness gradient model used to compute the predicted $\tau(p)$ values is given in Table 1.

The water column model is from the XSV data and the sediment model was obtained by traveltime inversion of data from 341.3 km long range propagation shot across the Pole Abyssal Plain (Duckworth, 1983). The parameters for the shots in line 1 are summarized in Table 2. This initial line was carried out before the entire

TABLE 1

Linear slowness gradient model used to compute the predicted $\tau(p)$ values

z (km)	c (km/s)
0	1.437
0.08	1.44
0.093	1.441
0.250	1.455
0.4	1.460
1.6	1.471
4.0	1.510
4.1	1.512
4.3	1.625
5	2.5

TABLE 2

Shot parameters for Fram 2 line 1

Charge weight (kg)	Depth @ rcvr (km)	Depth @ src (km)	Dip (deg.)	Range (BIO) (km)	Range (bounce) (km)	Bearing (true deg.)
25	4.025	3.86	-0.71	13.4	13.1	26
25	4.025	4.01	-0.05	18.9	18.9	20
25	4.025	4.01	-0.05	23	23.3	22
25	4.025	4.32	0.62	27.2	27.6	21
25	4.025	4.10	0.13	34.1	31.3	20
25	4.025	3.93	-0.13	41.1		20

24 channel array was operational and utilized only 18 sensors. A schematic view of the array coverage for line 1 is given in Fig. 4. It should be noted that the total offset coverage is quite sparse.

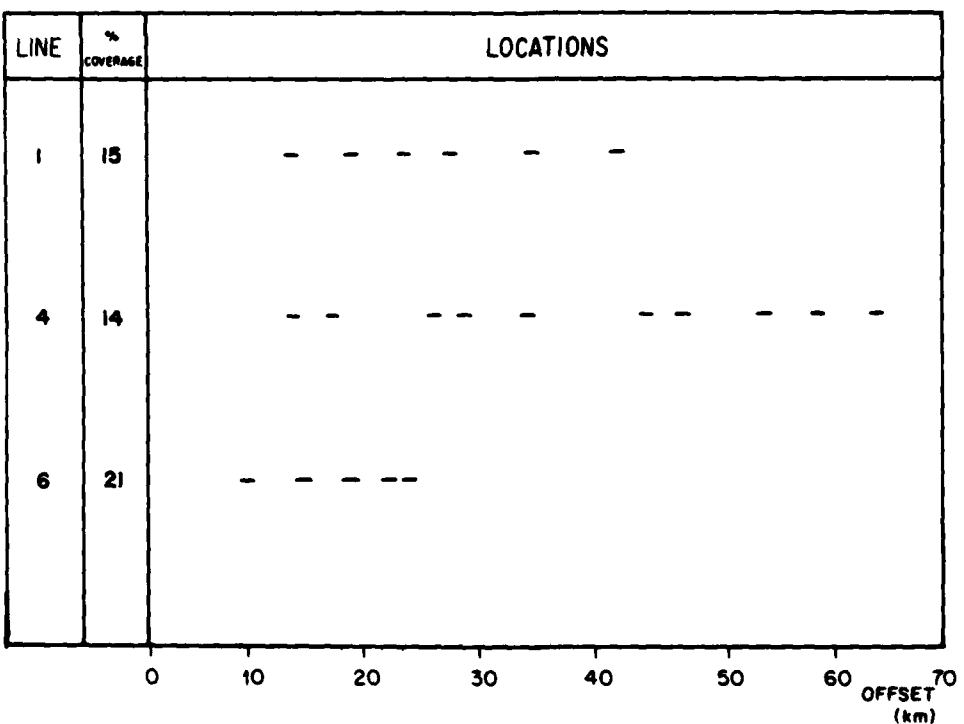


Fig. 4. Refraction line offset coverage for the Fram 2 experiment lines 1, 4, and 6.

Velocity spectra, τ - p spectra, and velocity/depth inversion

The velocity spectrum

The velocity spectrum is simply a measure of the power in the signal arriving at the array in a specified frequency band as a function of horizontal slowness, p , (the inverse of phase velocity) the arrival time, t . To acquaint the reader with the use of velocity spectral processing output, and how it compares to the waveforms themselves, two of the traces and their corresponding velocity spectrum for the 4 Hz band centered around 6 Hz are considered. Details of the velocity spectral processing procedure are available elsewhere (Baggeroer and Falconer, 1982; Duckworth et al., 1982; Duckworth, 1983). The example spectrum in Fig. 5 is from line 1 and has a reference offset of 27.2 km. This reference distance is approximately the midpoint of the projection of the 2-D array along the line of propagation from the shot, and is the range to the apex phone which was designated to be the reference point. The waveforms plotted at the top of the figures are lowpassed at 30 Hz and are taken at sensors 600 m apart to indicate the changes in waveform shape over the array aperture. The traces are uncorrected for moveout, and the top trace is the reference for the velocity spectrum. It should be noted that the data are exceptionally coherent and noise free for refraction data. This can be attributed to the quiet platform provided by the ice, the high dynamic range of the acquisition system and the large charge sizes employed (25 kg of TNT). As can be seen from the similar (and low) ambient noise levels preceding the initial arrival, the differences between the two traces in Figs. 5a-c are variations due to differential propagation paths for the sensors, not independent sensor noise. The arrival path identifications used in this example were made by first determining a model using much more data than this single shot. The predictions of this model were then compared to the arrivals at 27.2 km to make the identifications. One can not clearly assign paths based on observation of a single velocity spectrum alone. A complete discussion of the arrival structure in this velocity spectrum is given in the caption for Fig. 5.

There is an additional interesting structure imparted on the velocity spectra by near-surface multipath because high gradient regions can cause large changes in observed slowness for small changes in offset. Because the source and receivers are located 243 m and 93 m, respectively, below the surface of the ocean, each major event consists of a four arrival complex. Each of the four multipaths has a slightly different geometrical ray path, and thus samples the medium slightly differently. Initially, one would consider this added complexity to the data as just one more problem to deal with, and in many cases it is, since the elongated impulse response for one event can obscure other, weaker arrivals. However, the fine structure of these multipaths can be used to an advantage in the interpretation if the data are processed by the velocity spectral analysis algorithm. Figure 6a shows a hypothetical velocity/depth function. A simplified ray diagram showing only the multipaths at the source is given in Fig. 6b. Path 1 is the direct ray and path 2 is the ray that

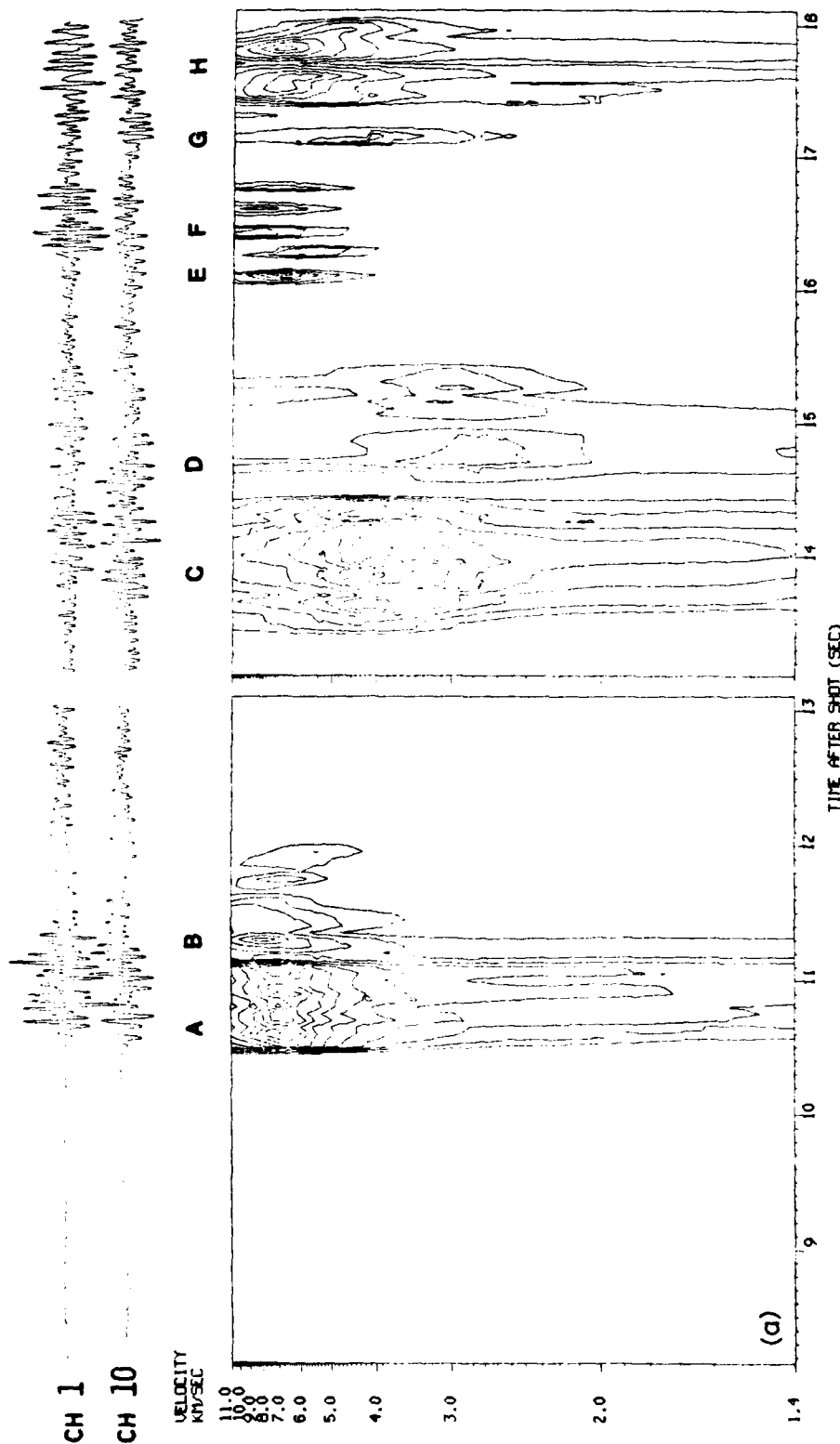


Fig. 5a. Waveform and 6 Hz velocity spectrum for Fram 2 seismic refraction experiment with source/receiver offset = 27.2 km. The waveforms are lowpassed at 30 Hz and are taken at sensors 600 m apart to indicate coherency. The traces are uncorrected for moveout, and the top trace is the reference for the velocity spectrum. For the spectrum, the contour intervals are 3 dB. For these panels the waveforms are plotted with a relative gain of 20 in amplitude. Event A is the layer 3 primary. The four peaks are due to surface reflections at the source and receiver. Event B is the Moho compressional arrival. Event C is a layer 3 shear primary arrival. Event D is a deep sediment compressional primary. Events E and F are layer 3 and Moho water column pleg multiples. Arrival G is a deep layer 2 second multiple, and event H is the layer 3 free surface multiple. Note that the events that are clearly delineated on the spectrum are not easily picked on the waveforms themselves.

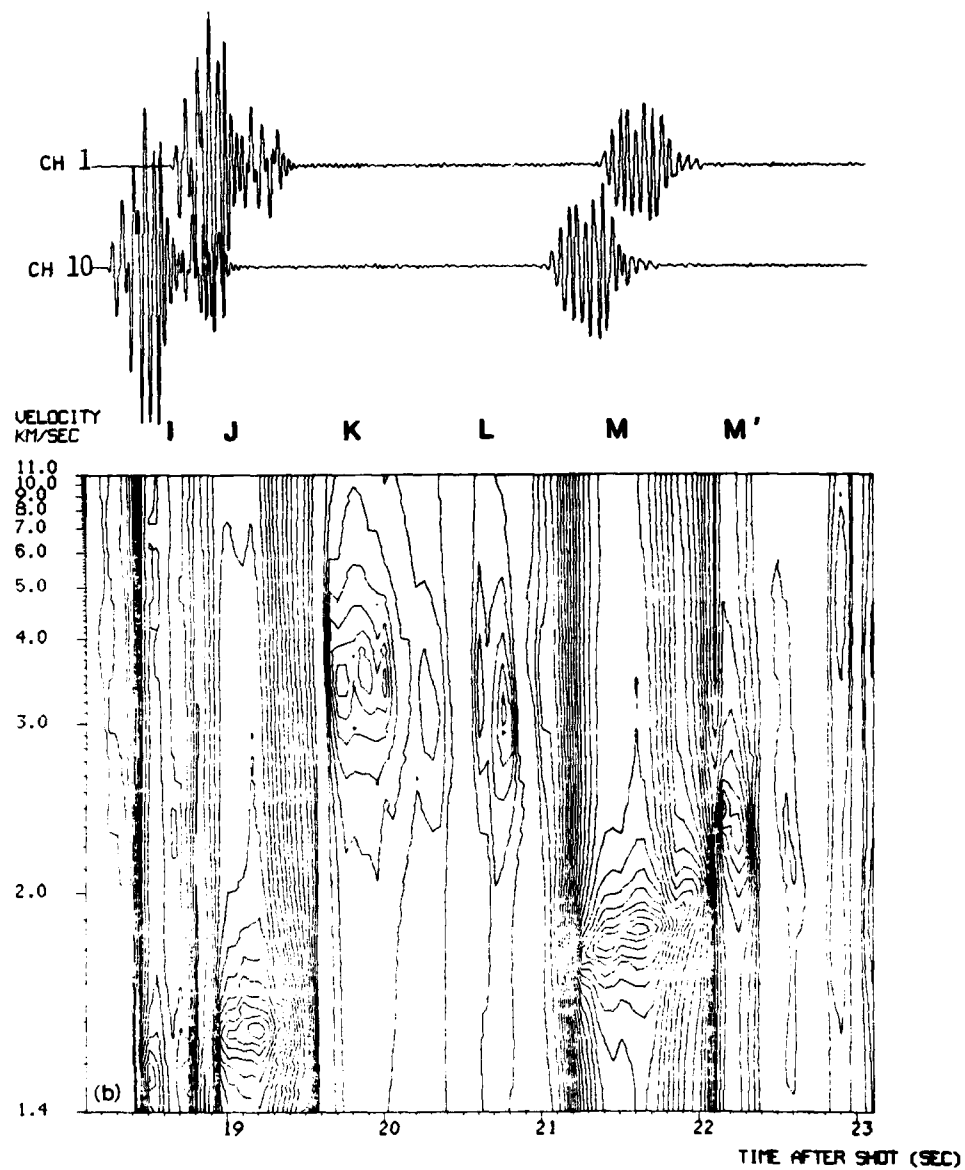


Fig. 5b. Waveform and velocity spectrum of Fig. 5a continued. The waveforms are plotted with a relative gain of 0.5 in amplitude. Event *I* is the direct water arrival. Note that at 27.2 km the offset is exactly half the distance to the first convergence zone and the arrival is relatively weak. Arrival *J* is the primary refraction from the upper sediments. Event *K* is the compressional arrival from the deeper sediments, and *L* is a shear multiple from layer 3. Complex *M* is the second free surface multiple from a sediment refraction path. A high sediment velocity gradient causes the rise in phase velocity as the near source/receiver free surface ghosts arrive. Event *M'* is probably the water column pegleg multiple for a deep sediment compressional path.

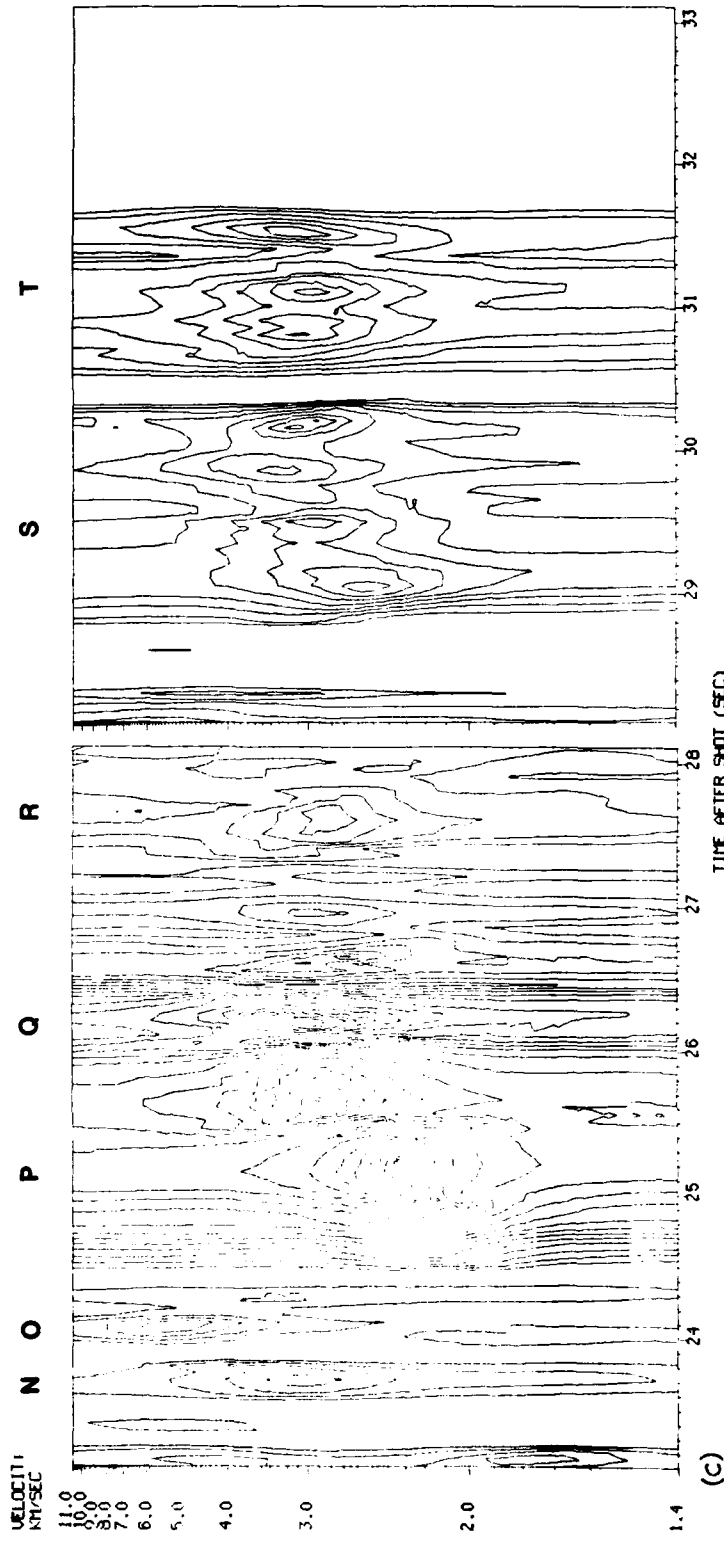
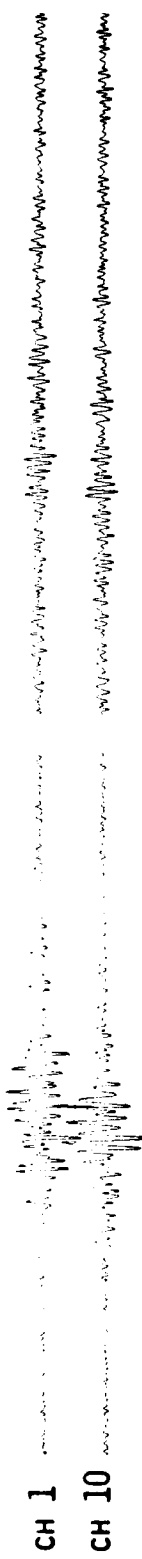


Fig. 5c. Waveform and velocity spectrum of Fig. 5a continued. The waveforms are plotted with a relative gain of 2.0 in amplitude for the first panel, and a relative gain of 5.0 for the second panel. Event N is an internal multiple of undetermined path. Arrival O is the layer 2 compressional third free surface multiple. The complex P is the third free surface multiple of the sediment refraction. The event labeled Q is probably a deep layer 2 shear path third free surface multiple. Weak arrival R is a shallower layer 2 shear third free surface multiple. Event S is a layer 2 shear path. Complex T is the sediment compressional refraction fourth free surface multiple.

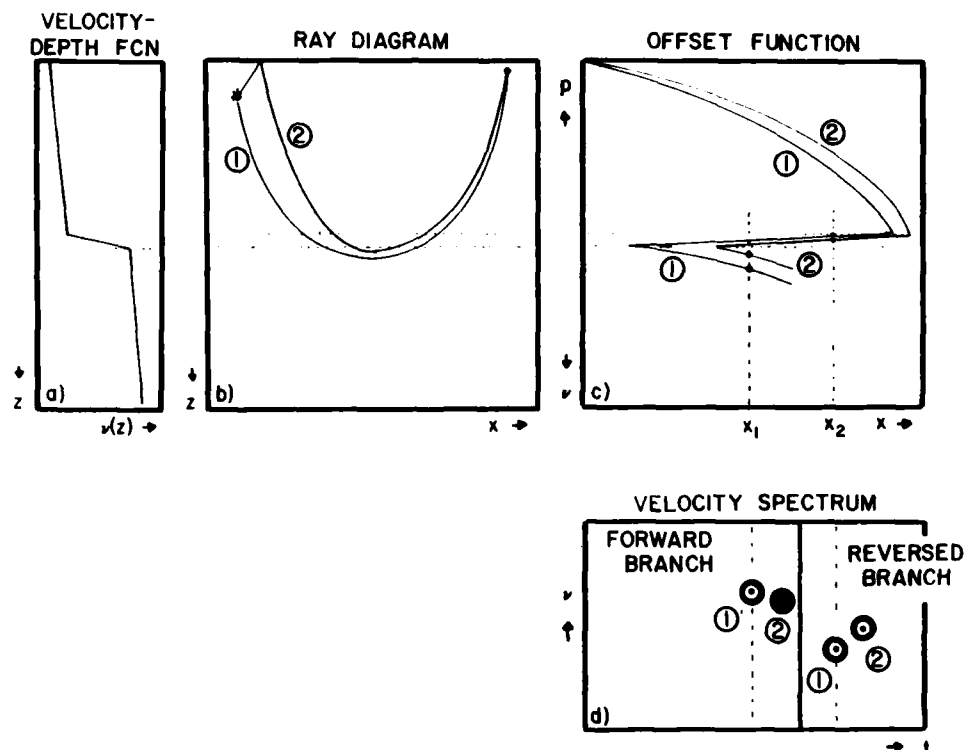


Fig. 6. Diagram indicating the features on the velocity spectral records due to near-surface multipaths. See text for discussion.

initially travels to the surface and is reflected * specularly. For moderate values of slowness, the effective offset is reduced by over 200 m, thus sampling a different region in slowness of the geometrical curves. A qualitative picture of the geometrical

* It was initially thought that the surface reflection at the source would be much less powerful than the direct arrival. The argument for this was that the peak pressure of the shock wave at the surface for a 25 kg charge detonated at 243 m was 231 dB re 1 μ Pa. Since ambient air pressure is 220 dB re 1 μ Pa, it was assumed that the reflected pulse would cavitate, and only a 220 dB reflection would be supported. However, experiments conducted by Weston (1960) indicated that the surface cavitation threshold for explosions was about 246 dB re 1 μ Pa, said to be due to the tensile strength of water for short duration stresses. In addition, in the Arctic another 2 dB is gained due to the depression of the water interface by the ice layer. Our data indicate that there is little loss in the surface reflection, and the reflection coefficient is well modeled by -1 at the frequencies of interest. The appearance of the thin (1-4 m) ice layer does not seem to complicate the reflection coefficient very much for the wavelengths of interest (50-300 m). A solid ice layer would seem to present a differentiator--the large positive reflection coefficient at the bottom of the ice (45), followed quickly by the -1 reflection coefficient at the free surface. However, other experiments indicate that the reflections from the bottom of the ice are quite small. This may be attributed to an impedance matching "slushy" layer at the bottom of sea ice. Many seismic refraction experiments have shot weight and depths which combine to produce surface pressures in excess of the 246 dB, so the surface reflection is attenuated.

offset function is given in Fig. 6c. By drawing lines at constant offset it can be seen that whether the traveltime curves are on a forward (low gradient) or reversed branch (high gradient) determines if the arrival corresponding to path 1 or 2 has a higher apparent velocity across the array. Finally, this can be translated to the velocity spectra (Fig. 6d) at the two offsets, x_1 and x_2 . The event labeled 2 will always have a larger arrival time due to the extra path to the surface. The structure of the arrival information in $t-p$ space is thus indicative of the gradient near the depth of the turning points. A good example of this appears in Fig. 5b. The arrival complex M is the second free surface multiple (two turning points at depth) from a sediment compressional refraction path. A high sediment velocity gradient causes a rise in phase velocity at the near source/receiver free surface ghosts arrive.

The $\tau-p$ spectrum

Obviously, identification of all the paths noted in Figs. 5a-c is not possible from the one velocity spectrum alone, especially not in the $t-p$ domain in which arrivals have no well-defined organization in terms of order of arrival. The procedure by which the identifications were made is roughly the following. First, the data from

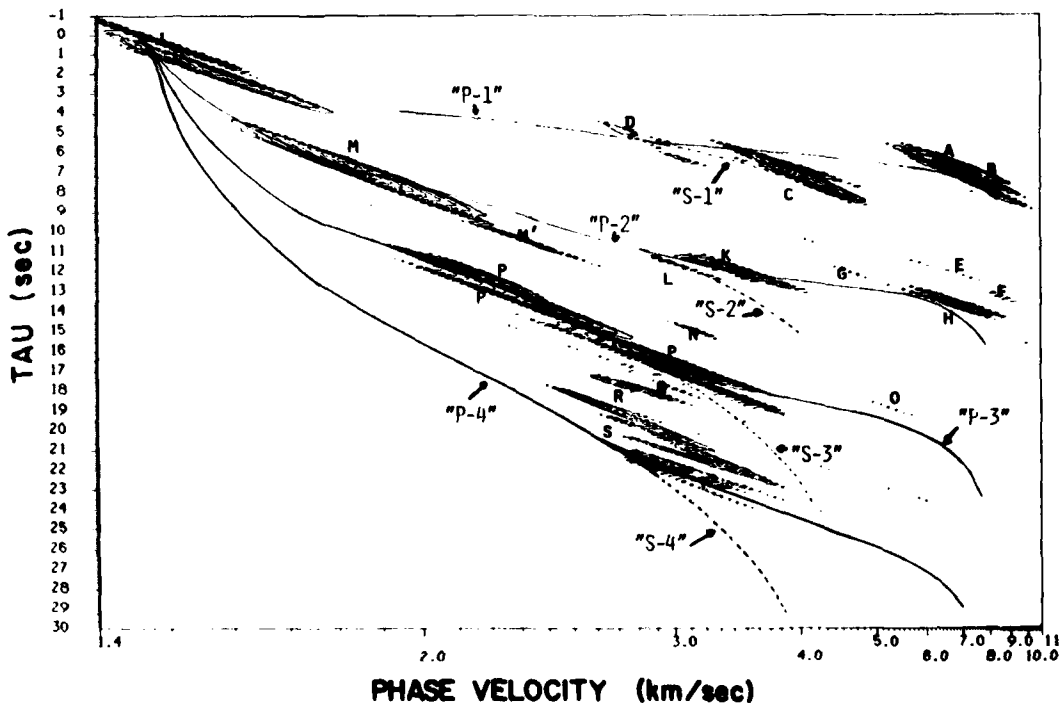
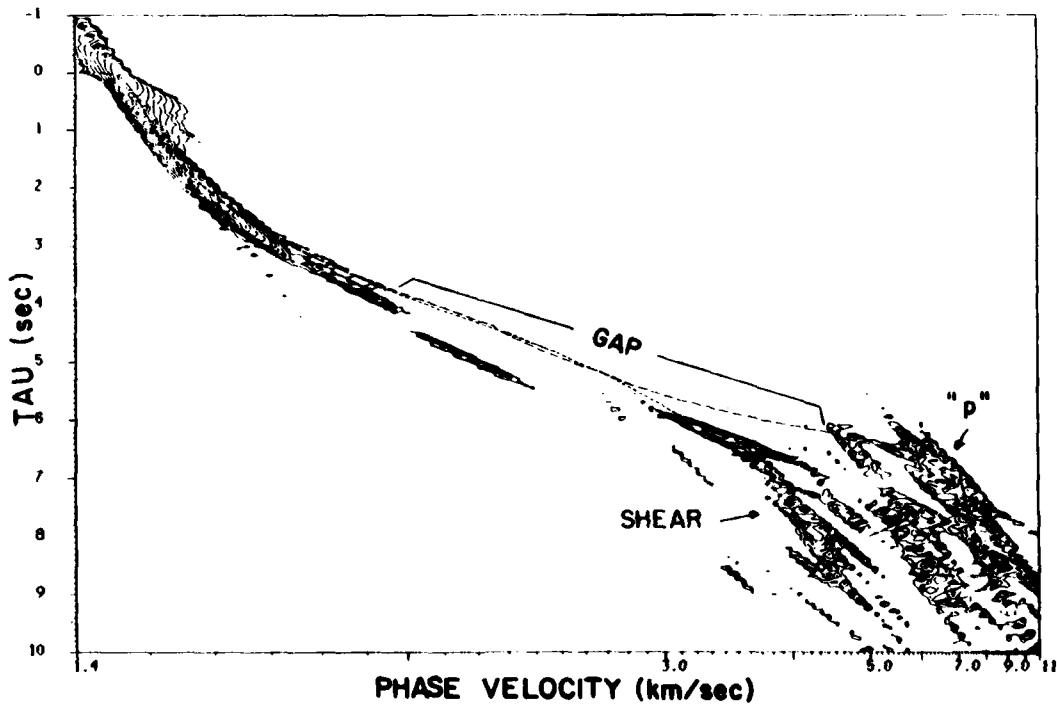


Fig. 7. τ -slowness spectrum at 6 Hz of the shot in Fig 5. τ -slowness from a possible model obtained from this and other shots is shown superposed on the spectrum. Solid lines are for the compressional model, dotted lines are curves for the shear model. The events indicated in Fig. 5 are labeled. Contour intervals are 10 dB.

this offset and frequency and other offsets and frequencies were converted to the τ - p domain using the coordinate transformation $\tau(p) = t(p) - px(p)$ on the velocity spectrum. The conversion of the velocity spectrum of Fig. 5 is given in Fig. 7. The events labeled on Fig. 5 are also noted there. The rough and complicated looking structure of the τ - p spectrum is due to two factors: using no interpolation when converting from the t - p to τ - p grid, and the use of a simplistic (but fast) contour plotter that crosses contours when it is confused by a saddle point in the data. The appearance of the contour plot is of little consequence because it has been found easier to use a gray-scale or color monitor when carrying out quantitative interactive manipulation of the spectra.

Since transformation to the τ - p domain removes the offset dependence of the velocity spectra, the τ - p spectra from the six offsets on this line can be composited. When only the primary arrivals are used, the result in Fig. 8 is obtained. For this plot the six shots of line 1 at 14 Hz have been combined, using a "largest of" rule, and are contoured at 10 dB intervals. The use of the value of the τ - p spectrum from the offset with the largest power value at any given τ - p point avoids summing the background noise. There is no benefit in trying to coherently add this power measure because the spectra from data at different offsets are expected to sample



in the line. The $\tau(p)$ curves for a possible model have been added to aid in interpretation of the arrivals. Contour intervals are 10 dB.

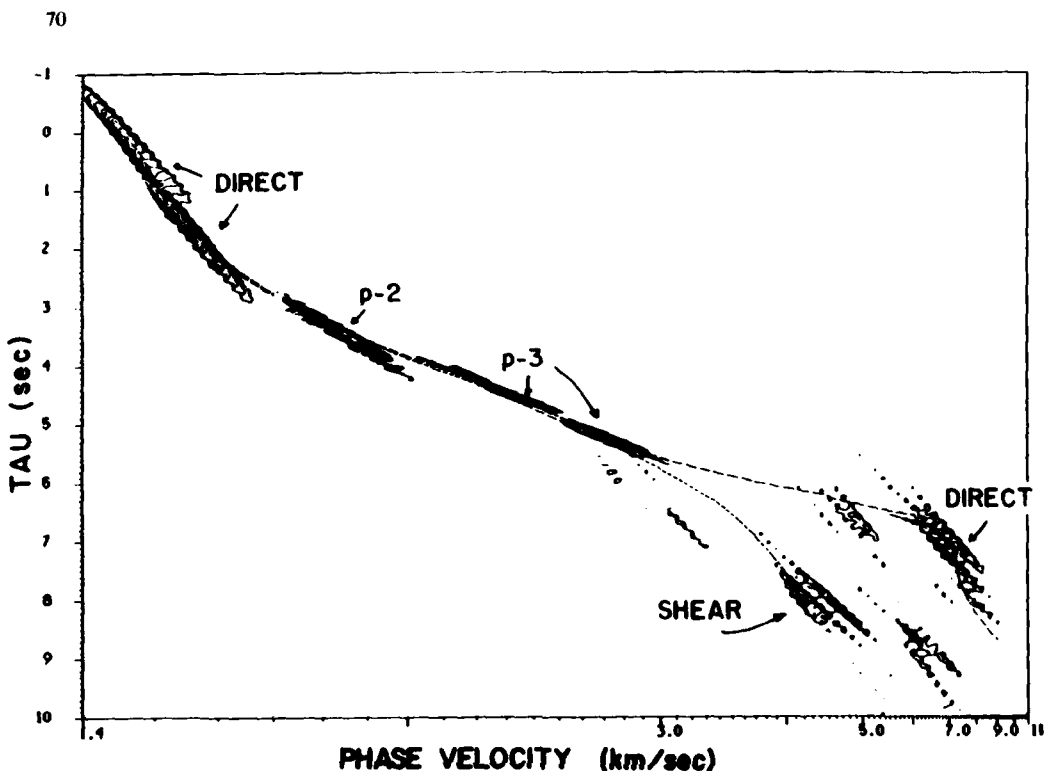


Fig. 9. The τ -slowness spectrum at 14 Hz for the shot in Fig. 5 after "condensing" the free surface multiples to their equivalent primary curves. Note, this plot is for one offset only, 27.2 km. The individual contributions of the different multiples have been labeled. Contour intervals are 10 dB.

different regions of the τ - p curve and the background level will rise with no increase in the height of the signal peaks. Note that because of the sparse offset sampling between the shot locations there is a large gap in the slowness coverage in the deep sediment to layer 2 region *.

These data alone would obviously lead to a very ambiguous model. The situation can, however, be greatly improved by utilizing the free surface multiples. Because a free-surface multiple of order N has N times the delay time τ of the primary **, a τ - p plot such as Fig. 7 can be used to identify the order of any given arrival quite easily. This "organization" of the arrivals afforded by the τ - p display domain is one of its primary advantages. The sorting out process is expedited by a display of the primary and multiple τ - p curves for a model which is known to be reasonable for the data. Once the multiplicity of a given arrival is known, it can be "condensed" back to the primary curve. This is carried out by the coordinate transformation on the appropriate region of the velocity or τ - p spectrum given by:

* The line curves on the plot are the τ - p loci for the model that will eventually be determined from inversion of these data.

** A small correction is needed for the depth of the source and receivers.

$$(t, \tau, p, x) \rightarrow \left(\frac{t}{N}, \frac{\tau}{N}, p, \frac{x}{N} \right)$$

In this manner, if horizontal homogeneity holds for the medium, a shot at 28 km can provide information that would be observed on primary arrivals at 14 and 9.3 km. The result of condensing the 14 Hz τ - p spectrum from an offset of 27.2 km is shown in Fig. 9. For this figure only the first two free surface multiples have been condensed, and are labeled as p -2 for the second free surface multiple (2 turning points), and p -3 for the third free surface multiple (3 turning points).

When this procedure is carried out for the six shots of line 1, the resulting composite τ - p spectrum for a center frequency of 14 Hz in Fig. 10 is obtained. Utilization of all the multiples results in a very densely sampled τ - p curve. An interesting thing to note from Fig. 10 is that the lack of compressional arrivals in the velocity region from 3.0 to 4.5 km/s corresponds to a region in which strong shear arrivals break away from the compressional curve. This indicates that there is probably a smooth basement with a strong compressional velocity contrast at the base of the sediments, favoring P to S conversions. The weak contrast between what appears to be a thin, high velocity, layer 2 and layer 3 yields strong layer 3 shear

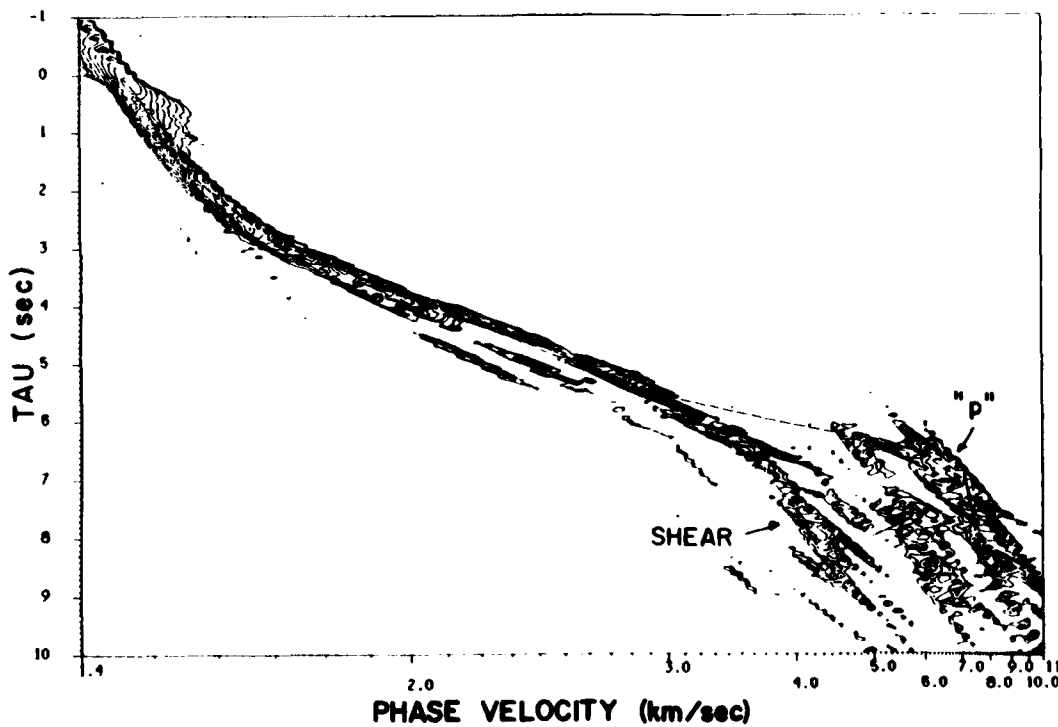


Fig. 10. The 14 Hz τ -slowness spectrum with all six shots and all multiples "condensed" to the primary curve. Contour intervals are 10 dB.

arrivals in the 2.9 to 4.4 km/s range. Although not pictured here, support for the validity of compositing the multiples is given by the fact that the second free surface multiple data for this shot at 27.2 km looks almost identical to the primary data at an offset of 13.4 km.

Inversion of the τ - p spectrum

The wavefield continuation or velocity/depth "migration" technique proposed by Clayton and McMechan (1981) can be used to image the velocity/depth function from the τ - p spectra. One advantage of using τ - p data obtained in this manner over that obtained from a conventional slant stack is its insensitivity to phase shifts. Because this method provides a power spectrum, it is insensitive to the phase shifts in the data introduced by postcritical reflections and gradient refractions (Duckworth, 1983). In Fig. 11 the data from 27.2 km (Fig. 9) are imaged by the model determined through a τ -sum inversion of a τ - p curve for a homogeneous layered model (Diebold and Stoffa, 1981). The peaks appear to image onto the trial model quite well, the condition for completion of the inversion. The image of the data from all offsets and multiples migrated by the compressional wave velocity profile is

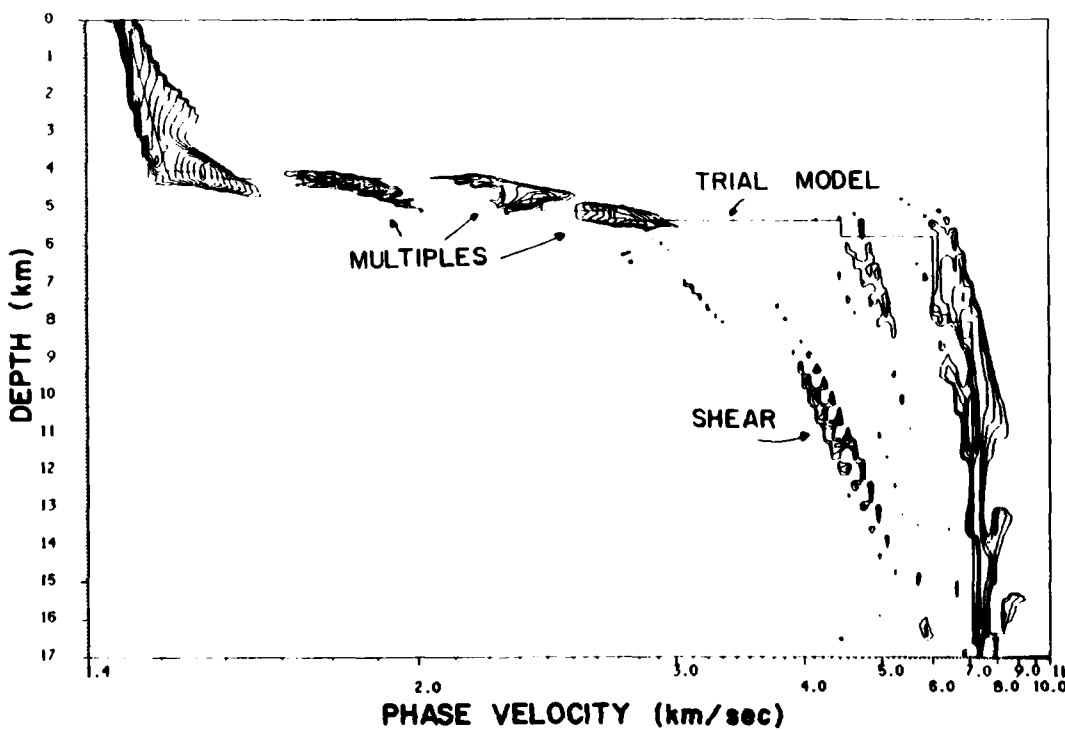


Fig. 11. Compressional velocity/depth migration image of τ -slowness spectrum of Fig. 7 after condensing all multiples from 27.2 km. Contour intervals are 10 dB.

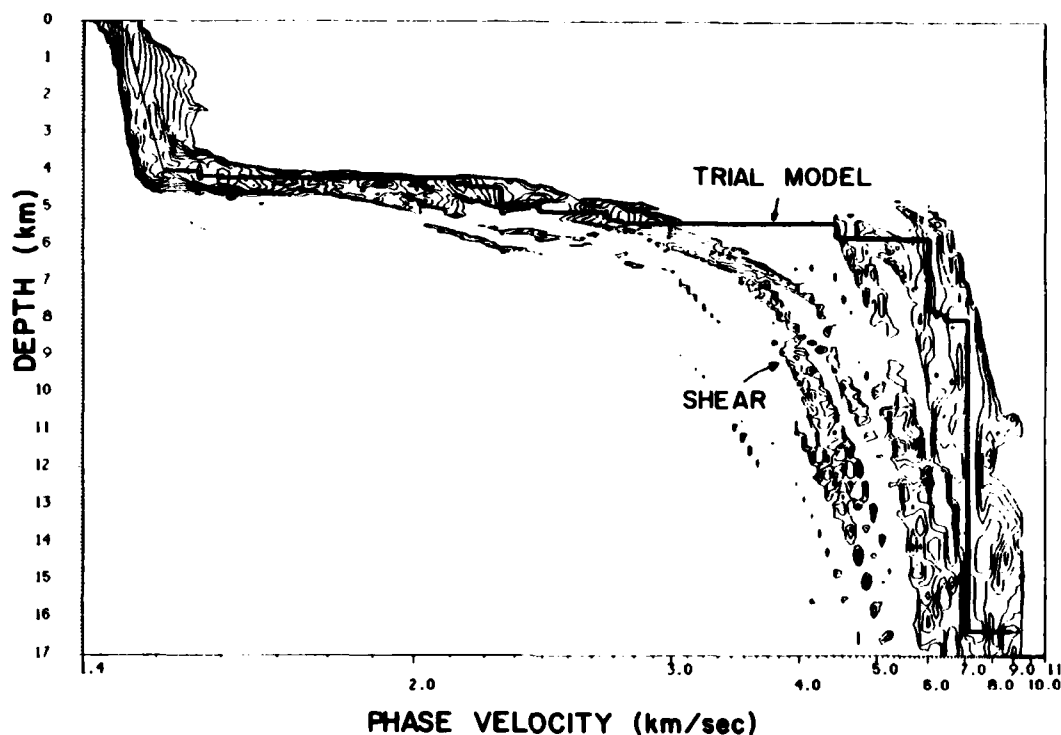


Fig. 12. Compressional velocity/depth migration image of τ -slowness spectrum of Fig. 10 consisting of all multiples from all six offsets in line 1 at 14 Hz. Contour intervals are 10 dB.

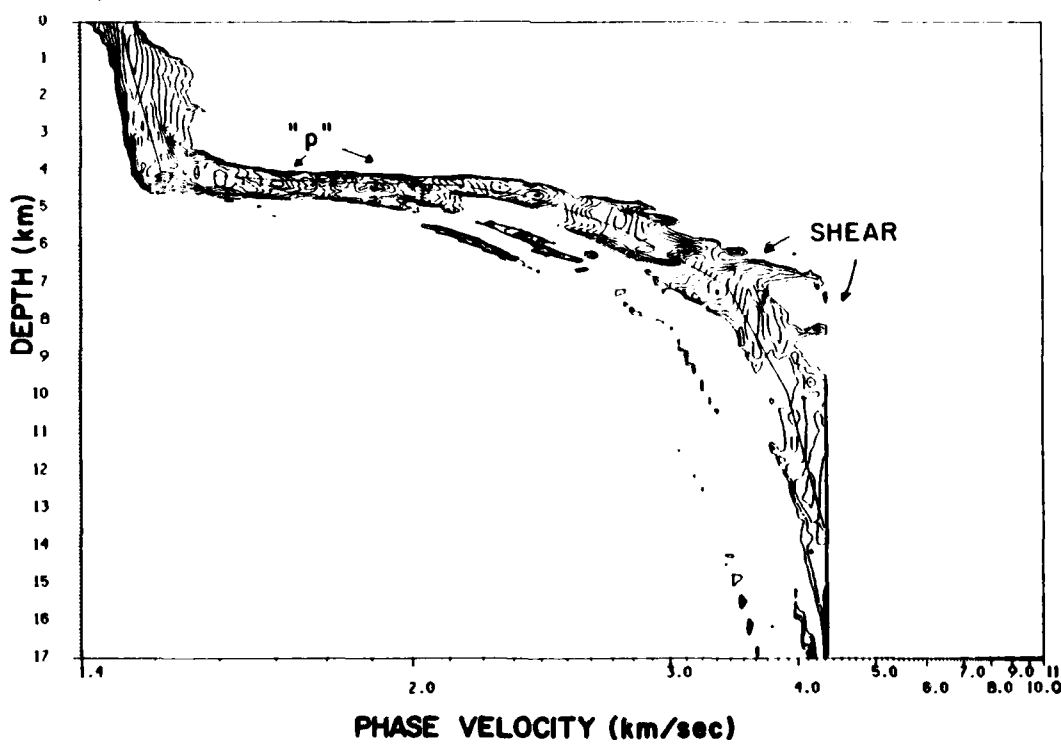


Fig. 13. Shear wave velocity/depth migration image of Fig. 10 consisting of all multiples from all six offsets in line 1 at 14 Hz. Contour intervals are 10 dB.

shown in Fig. 12. Figure 13 gives the image of all the data after migrating with a trial shear profile below the conversion at the base of the sediments (about 5 km below the ocean surface).

In Fig. 14 the models are plotted without the confusion of the imaged data. The compressional model plotted is the result of the τ -sum inversion which was verified by the migration. The shear model was obtained independently by use of the migration algorithm only, and is thus parameterized differently. Note that the resolution of the data is inadequate to distinguish between the gradient and homogeneously layered models for the compressional paths in the sediment. Amplitude studies should be used to refine the models; however, offset data given later will indicate that a gradient model is more appropriate in most cases. Finally, the dashed lines give extremal bounds on the model computed using the method of Bessonova et al. (1974) assuming an uncertainty of ± 0.1 sec in the τ data values.

One of the important points of this example is to show that the multichannel data and the velocity spectra identify many more events and features in the data from a single source/receiver offset than just the first arrival detection often done in

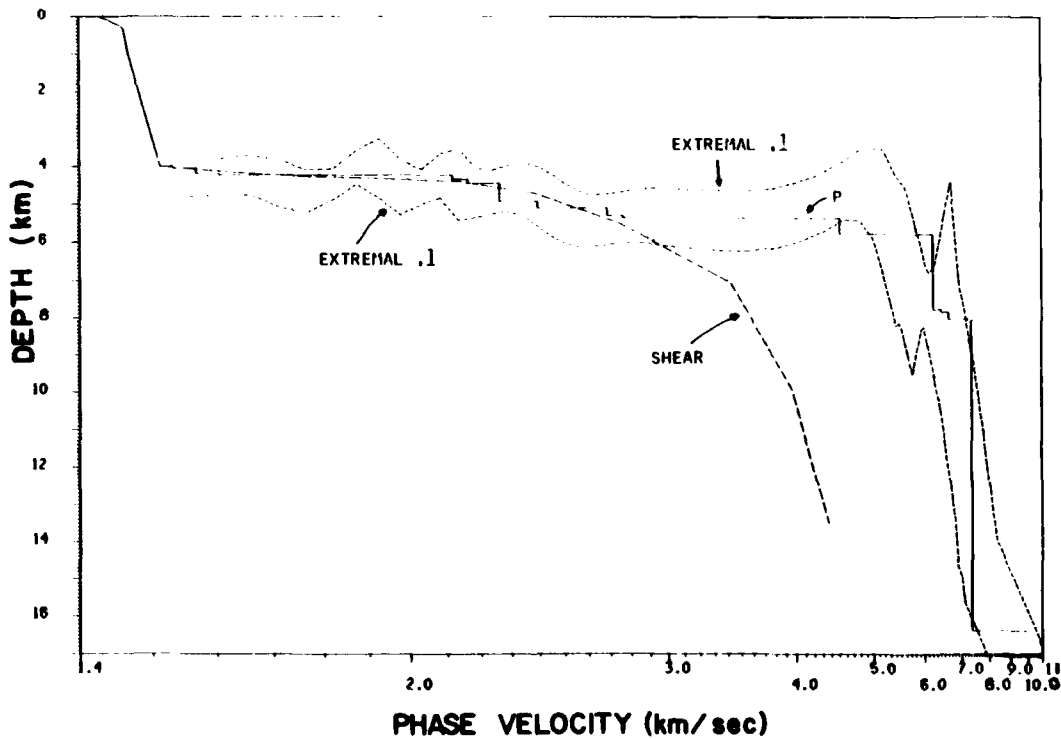


Fig. 14. Summary of the profiles obtained in this example. The solid curve labeled "P" is a possible compressional profile, and the dashed curve marked SHEAR is a possible shear profile. The curves marked EXTREMAL.1 are the extremal bounds determined by the method of Bessonova et al. (1974).

refraction analysis. In addition, the phase velocity, or its inverse, horizontal slowness, are directly estimated from the data when arrays are used. These additional identifications are especially useful in filling in the gaps in the offset coverage imposed by the ice cover.

The picked τ and offset data

In the previous section it was shown that velocity/depth migration could be carried out on the τ - p spectra. A major advantage of this technique is that the bandwidth and resolution inherent in the τ - p data are preserved in the width of the imaged velocity/depth section. However, the spectra are large datasets and are expensive and time consuming to generate, manipulate, and migrate. For example, the transformation from the velocity spectrum ($t, p: f, x$) to τ - p spectrum requires interpolation during the rotation to $(\tau, p: f)$ coordinates. The superposition of these spectra from different offsets and the reduction of multiples requires further manipulation of the large images. In addition, an image processing step is required to remove the well behaved, but existing, sidelobes from the velocity spectra. The sidelobes occupy the area between $t = t_0 - p_0 x_{\min}$ and $t = t_0 - p_0 x_{\max}$ for an arrival at (t_0, p_0) . The sidelobes appear as vertical stripes on the velocity spectra since x_{\max} and x_{\min} are the endpoints of the small (1 km) aperture of the array projected along the direction of propagation and centered around zero. However, after rotation to (τ, p) coordinates, the sidelobes form long streaks across the τ - p spectrum, with slopes given by the negative of the nominal offset of the shot. These artifacts can mask the weaker parts of the τ - p curve. One of the advantages of computing the t - p velocity spectrum before rotating to τ - p space is that the vertically oriented sidelobes are easier to remove by a simple image processing algorithm. However, to avoid the extra (though sometimes useful) work of manipulating the entire spectra, it is easiest to pick the peaks in $(t, p: f, x)$ space from the velocity spectra with a numerical 2-D gradient search algorithm. The algorithm implemented the first difference approximation to the gradient and generated contour maps of the data with the local maxima indicated on them. Although power thresholding was done to eliminate the peaks from local maxima in regions of background noise, it was necessary to use an interactive program to eliminate other spurious peaks. By this method, a table of peak power, time of arrival, t , slowness, p , and offset, x , was obtained for each frequency. This table was then corrected to the surface datum using the known water column profile above the source and receiver. The data in the table could then be readily manipulated to give $\tau(p)$ and $x(p)$ curves.

A plot of the corrected peaks corresponding to compressional arrivals at 6 Hz is given in Fig. 15a. Note that some surface ghosts are present in these data, thus increasing their apparent spread in τ and x . The 6 Hz data contributing to the "shear" path (some of which is compressional before the conversion at the base of the sediments) are plotted in Fig. 15b. The plots for other center frequencies are similar, with fewer detectable arrivals present on the highest frequency data, 18 Hz.

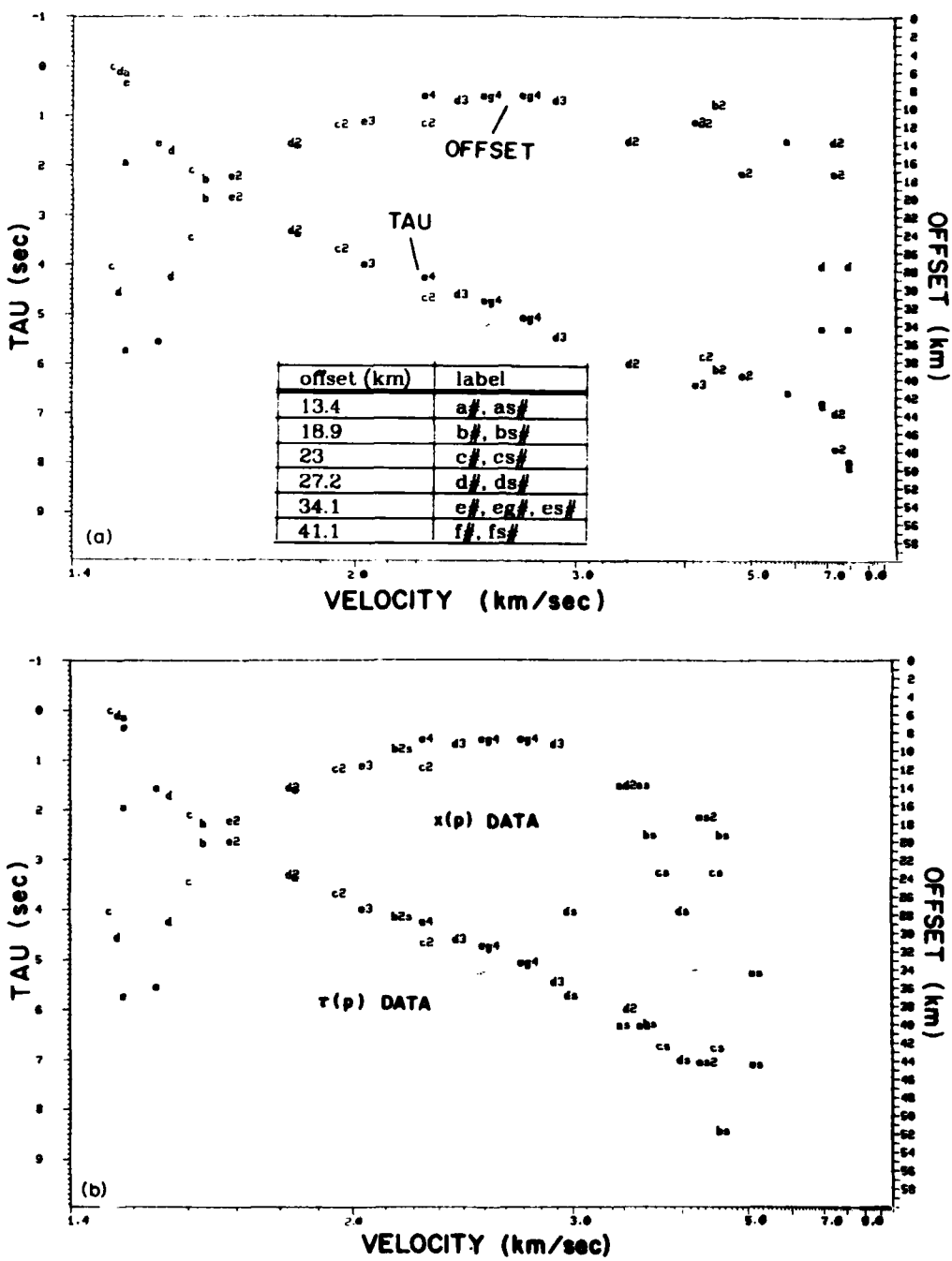


Fig. 15. Plot of the compressional $\tau(p)$ and $x(p)$ data picked from the velocity spectra of line 1 at a 6 Hz center frequency. The legend for the letter codes is given in the table. The number following the letter code is the order of the multiple. b. Plot of the shear path $\tau(p)$ and $x(p)$ data picked from the velocity spectra of line 1 at a 6 Hz center frequency. Same coding as in Fig. 15a.

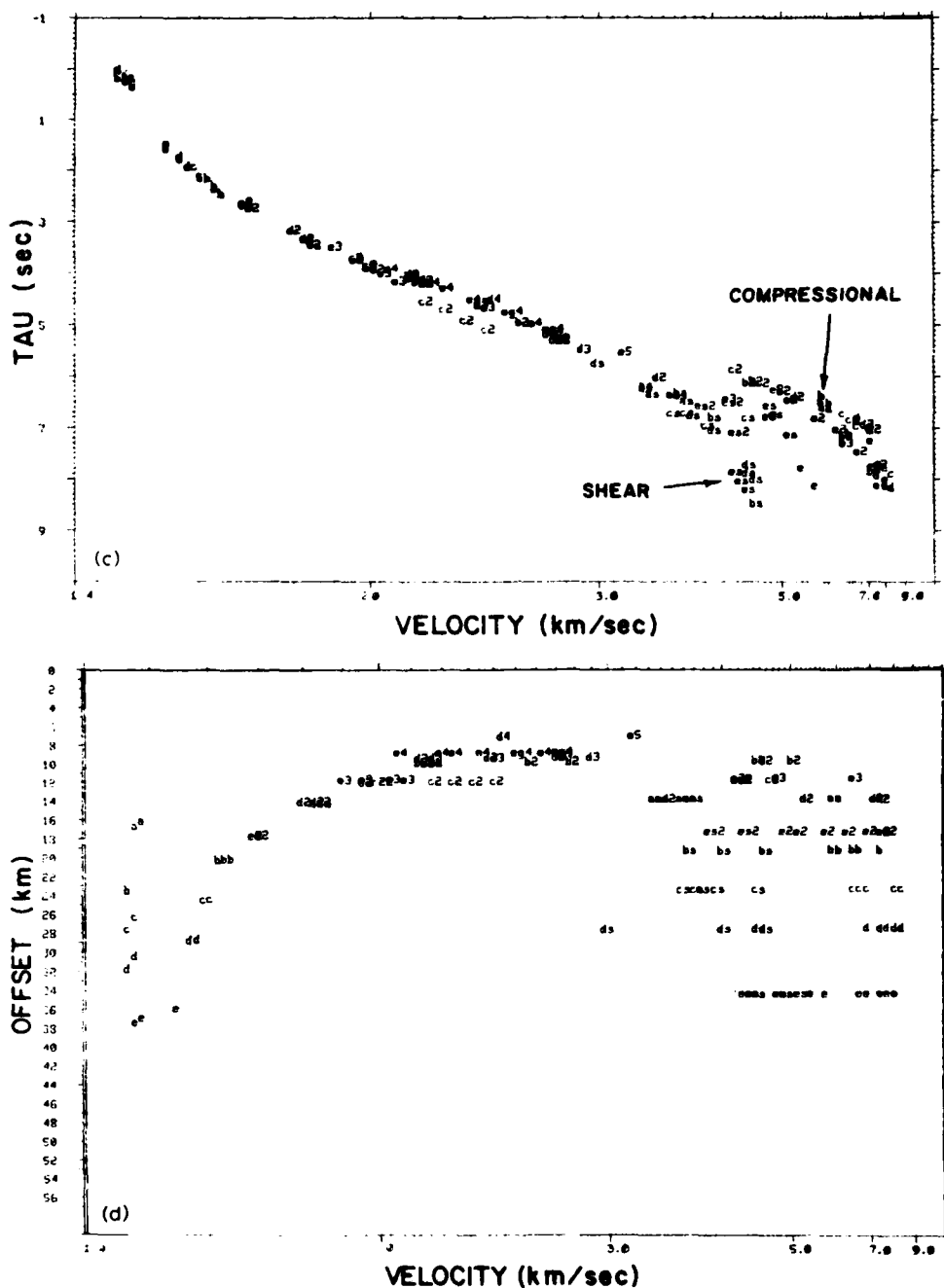


Fig. 15. c. Plot of the compressional and shear $\tau(p)$ data picked from the velocity spectra of line 1. This plot is the composite of the data at 6, 10, 14, and 18 Hz center frequencies and has had the free surface multiples reduced to the primary curve by the "condensing" procedure described in the text. d. Plot of the compressional and shear $x(p)$ data picked from the velocity spectra of line 1. This plot is the composite of the data at 6, 10, 14, and 18 Hz center frequencies and has had the free surface multiples reduced to the primary curve by the "condensing" procedure described in the text.

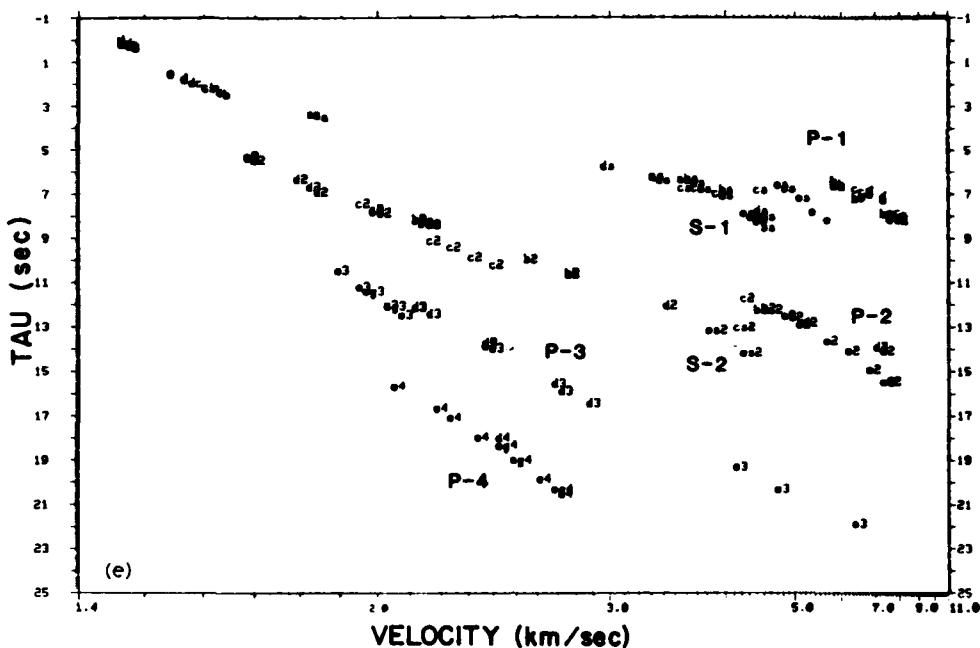


Fig. 15. e. Plot of the compressional and shear $\tau(p)$ data picked from the velocity spectra of line 1. This plot is the composite of the data at 6, 10, 14, and 18 Hz center frequencies. The data are "uncondensed" to show the order of the multiples that may be detected by the velocity spectral processing. The labels $P-1$, $S-1$, etc. correspond to the compressional and shear arrivals with 1 turning point, etc.

due to increased attenuation by the apparent Q of the medium. The τ and x curves after reduction to the primary arrival curves and composited over all frequencies are shown in Figs. 15c and d. As with the $\tau-p$ migration example given in the example above, there is a paucity of compressional arrivals in the layer 2 velocity region.

Finally, to show the order of the multiples, and the ranges (given by the letter codes in Fig. 15a) at which each type of multiple can be detected, a plot of the "uncondensed" $\tau(p)$ data is given in Fig. 15e. This plot contains both the compressional and shear data picked from the velocity spectra of line 1. This plot is the composite of the data at 6, 10, 14, and 18 Hz center frequencies. It is easily seen that without the use of multiples, large sections of the $\tau-p$ curve would be undefined.

Inversions by the τ -sum method

The τ -sum method proposed by Diebold and Stoffa (1981) is perhaps the easiest inversion method to understand, computer code, and use. The initial data analysis for line 1 was carried out using this method, and was reported by Duckworth et al. (1982). The models determined using this method are repeated in Fig. 16. For this analysis, the data at different center frequencies were treated separately, thus yielding the suite of models in the figure. The spread in the models is indicative of

the uncertainty in the data. Note that although there is some variability, the sediments start with an initially moderate gradient (0.6 s^{-1}) for the upper 0.3 km, then increase in gradient very sharply, perhaps even having a velocity discontinuity to about 1.9 km/s at 0.4 km into the sediments, then exhibit a gradient of 1.8 s^{-1} down to a depth of 5 km. As discussed before, there is evidence of a large velocity discontinuity at the basement interface, or at least a very high gradient. The τ -sum inversions bear this out; however, since there are no compressional data observed in this velocity region, it is impossible to tell unequivocally. It is a property of the τ -sum inversion for homogeneous layers that a large slowness gap in the data will be interpolated by a large velocity jump. It might help to have direct observations at offsets smaller than those observed; however, the shear conversion may be quite efficient and leave little compressional energy at these slownesses. The models in Fig. 16 indicate that the layer 2 region is approximately 0.5 km thick and has a velocity of 4.5 km/s. This is underlain by a layer 3 region with a velocity from 6 to 7.2 km/s, an initial gradient of 0.4 s^{-1} , and a total thickness of 2.5 to 6 km. The Moho depth is not well constrained by this line. To indicate how the model predicts the $\tau(p)$ data, Fig. 17 shows the 14 Hz data and $\tau(p)$ curve predicted by the 14 Hz model. The solid lines in the figure show the interpolating quarter ellipses character-

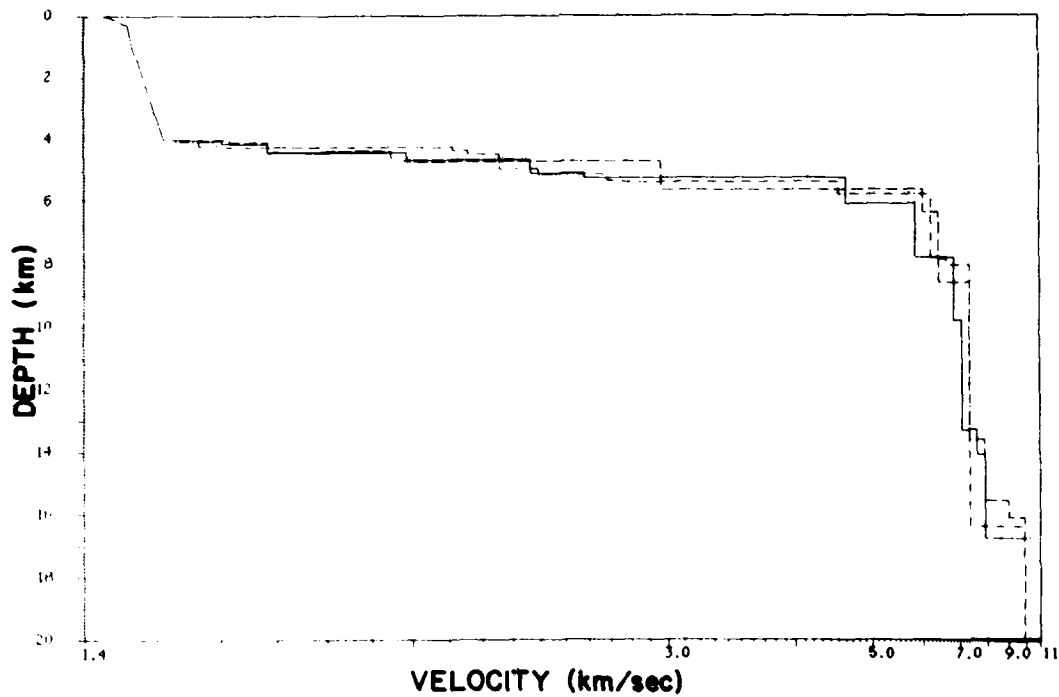


Fig. 16. The models resulting from inversion of the line 1 data using the homogeneous layered formulation of the τ -sum method. The 6 Hz data are indicated by the solid curve, the 10 Hz data by the dotted curve, the 14 Hz data by the dot-dashed curve, and the 18 Hz data by the dashed curve.

istic of the homogeneous layered model. The letters use the same system as outlined on Fig. 15; however, the upper case letters indicate arrivals that have less power, and are thus less reliable.

Inversions by velocity / depth migration

The migration example given earlier showed (see Figs. 7-13) that one of the models determined by the τ -sum method for the compressional profile imaged the $\tau(p)$ spectrum reasonably well, certainly within the resolution inherent in the bandwidth of the data. In this section the peaks picked from the data are imaged. For this work both the $\tau(p)$ and $x(p)$ data will be used to constrain the models resulting from the sparsely sampled slowness data curves. It has been shown that the use of both types of data leads to more tightly constrained models (Dorman and Jacobson, 1981).

Before giving the intermediate steps in the determination of the models, Fig. 18 summarizes the results of migrating the peak $\tau(p)$ and $x(p)$ data to obtain the compressional profile. Again, the curves for each center frequency were analyzed separately. In some cases more than one model was hypothesized for each frequency when one model was not clearly better than another. The results are an envelope of

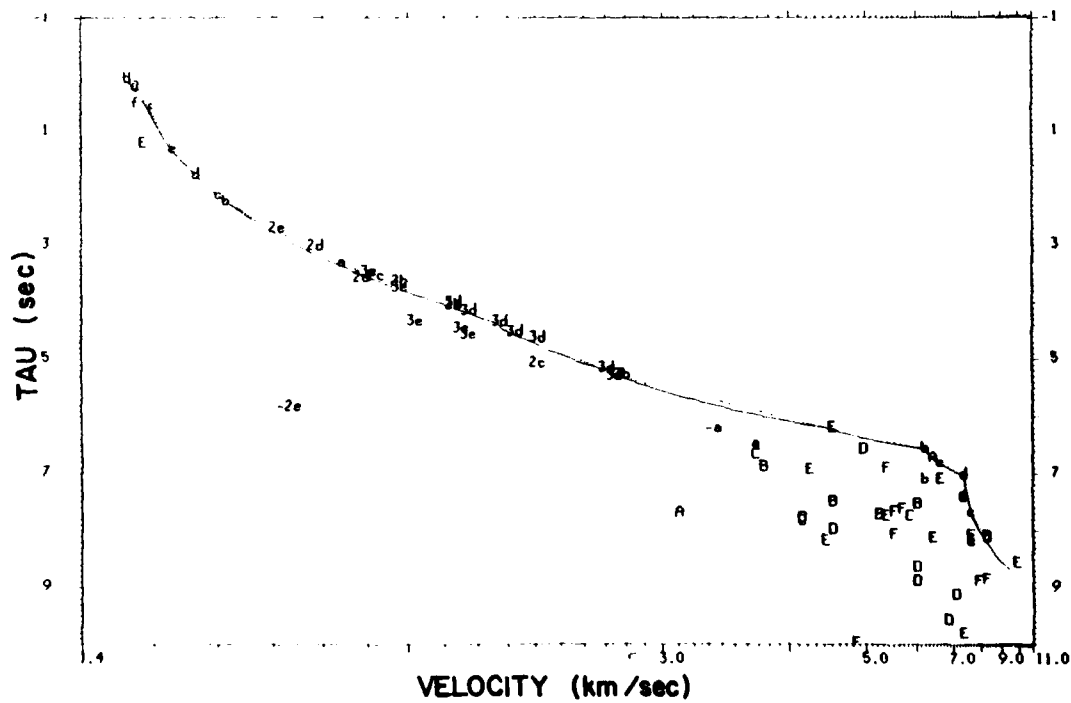


Fig. 17. The $\tau(p)$ data for 14 Hz (letter labels) and the curve predicted by the resulting model (solid line). The light dotted line interpolates the data points that were used in the inversion.

possible models indicating the resolution of the method. The models obtained agree well with those obtained by the τ -sum method. The major features are again the very high gradient in the middle of the sediments, followed by a more moderate one down to basement at 5–5.2 km total depth (1–1.2 km of sediments). A high gradient or discontinuity is indicated at this depth up to the basement velocity of 4.3–4.5 km/s. Layer 2 appears to be less than 1 km thick, and appears to have a gradient which is moderately high. This is difficult to say with confidence because of the paucity of compressional arrivals; however, it leads to the best overall agreement with both the τ and offset data in the slowness regions observed. Since the effective sampling is poorest at offsets less than 13 km, and no layer 2 arrivals appear at larger offsets, we assume that they must reside there. Such small offsets are indicative of high-velocity gradients leading to reversed branches of the travelttime curve. The gradient and thickness for layer 3 velocities are similar to that obtained by the previous analysis, and the total thickness of layer 3 averages about 4–5 km. The major difference between this profile and that obtained from the τ -sum technique is the omission of the lower gradient layer at the top of the sedimentary column. The imaged peak plots will show; however, that the offset data do indicate the need for this lower gradient layer. Note that one of the models in the suite has a

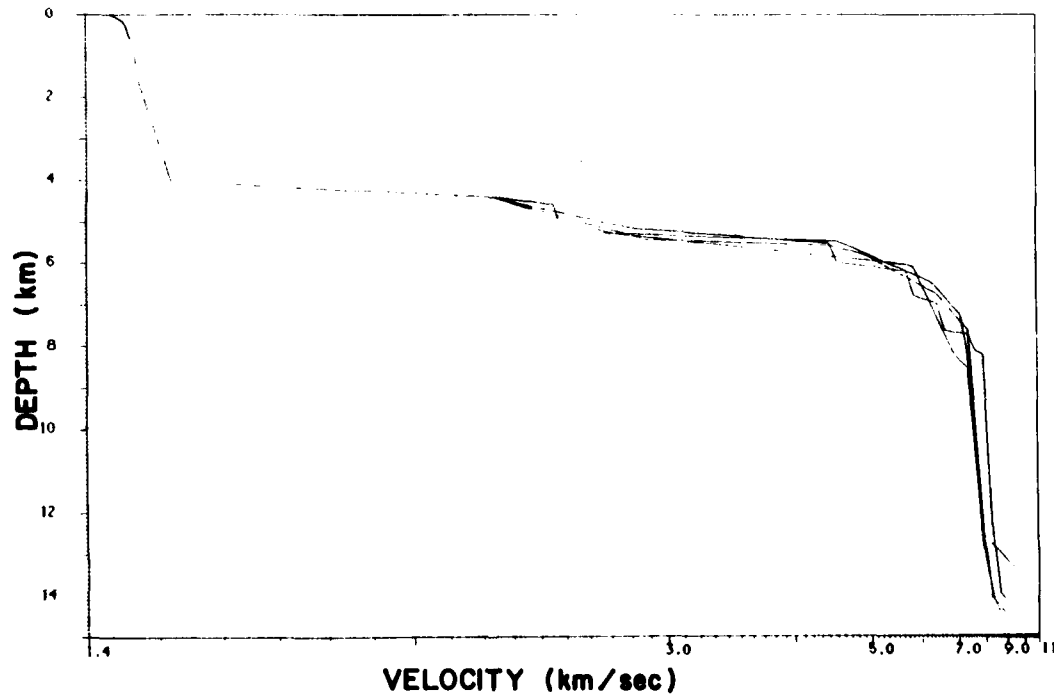


Fig. 18. The suite of compressional models resulting from the inversion of the $\tau(p)$ and $x(p)$ peak data. The inversion was carried out at individual center frequencies using the velocity/depth migration algorithm.

stair-step appearance, similar to a homogeneous layered model. Arrivals at velocities typical of layer 3 appear over large ranges in offset, indicating rapid changes in gradient with depth. The slowness stability of the velocity spectral estimator was not adequate to develop a consistent $x(p)$ curve that could actually determine the velocity discontinuities; however, it is worthwhile noting that such discontinuities are not inconsistent with the data. This complex layer 3 structure has been noted by other investigators (Spudich and Orcutt, 1980).

The shear wave velocity-depth profiles obtained below the conversion depth at the basement interface are shown in Fig. 19. Again, each frequency has been imaged separately and a suite of curves is obtained indicating the range of models that fit the data reasonably. These models are compared with the shear wave profiles predicted by using the compressional models of Fig. 18 and assuming a Poisson's ratio of $\sigma = 0.25$ in Fig. 19. The estimated shear profiles indicate that the crust is generally "less rigid" than a Poisson solid, with the measured shear profiles being generally of lower velocity than the predictions. Using the averages of the P and S

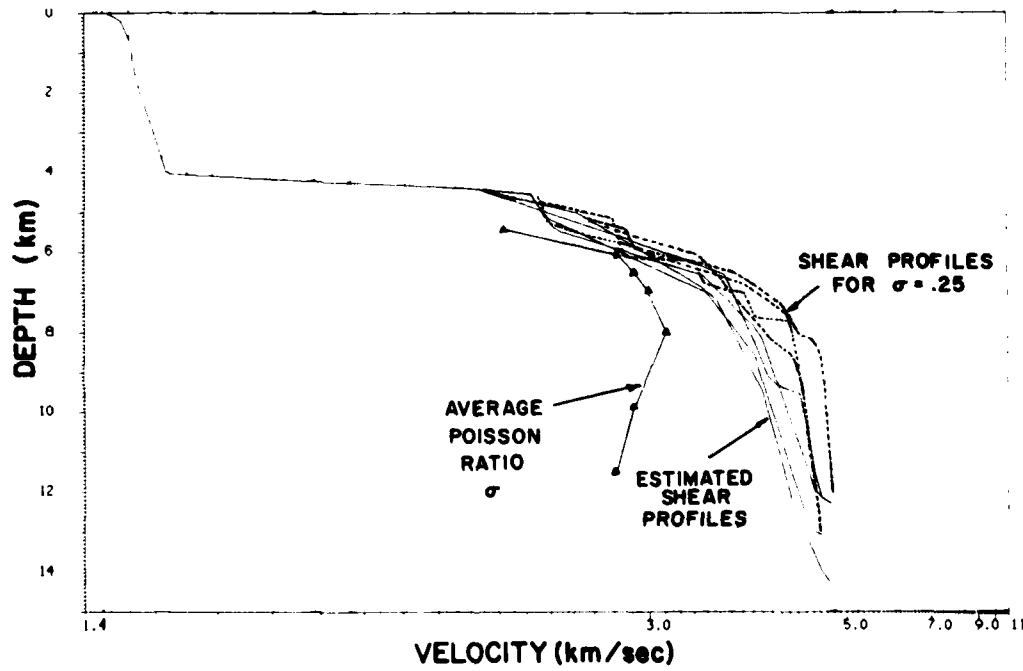


Fig. 19. The suite of shear velocity models (solid curves) resulting from the inversion of the $\tau(p)$ and $x(p)$ peak data. The inversion was carried out at individual center frequencies using the velocity/depth migration algorithm. Also shown is the suite of shear wave models obtained from the compressional models of Fig. 18 assuming a Poisson's ratio of $\sigma = 0.25$ (dotted curves). The solid line with triangles is the Poisson's ratio calculated for the crustal model obtained by averaging the suite of estimated compressional and shear models. The scale for σ is the velocity scale divided by 10.

TABLE 3
Average values of Poisson's ratio for Fram 2 line 1

Depth (km)	V_p (km/s)	V_s (km/s)	Poissons ratio σ
5.5	4.5	2.65	0.23
6	5.5	3.05	0.28
6.5	6.1	3.3	0.29
7	6.5	3.5	0.3
8	7.2	3.75	0.31
9	7.6	4.15	0.29
11.5	8	4.4	0.28

velocity profiles in Fig. 19 gives the estimate of the Poisson's ratio from the relation:

$$\sigma = \frac{\left[(V_p/V_s)^2/2 \right] - 1}{(V_p/V_s)^2 - 1}$$

where V_p is the compressional velocity, and V_s is the shear velocity at a given depth (Bott, 1982). The values obtained agree well with those tabulated from the literature by Christensen and Salisbury (1975) and support a gabbroic petrology for layer 3, a popular interpretation (e.g. Christensen and Salisbury, 1975; Bott, 1982). These are plotted as the triangles with connecting lines in Fig. 19. The values are also tabulated in Table 3.

The impossibly low σ for the 5.5 km depth is a result of being near the conversion region from compressional to shear, and a mixture of P and S paths in the upper basement due to topography could be the source of this artificially low ratio.

To indicate how the velocity/depth migration works, we examine a few of the plots of migrated peaks, and the predicted τ and x values vs. those of the data. Figure 20 gives one of the trial models (heavy solid line) and the results of imaging the 14 Hz compressional peaks. The set of lower case letters connected by the dotted line is the image of the $\tau(p)$ peaks. The set of upper case letters is the corresponding migrated image of the offset data. At the base of the water column the image of the $x(p)$ data indicates that the gradient is too large, leading to an image of the offset data which is too deep (Duckworth, 1983). The image of the $\tau(p)$ data also reflects this, but not so dramatically. This agrees with the analysis of Dorman and Jacobson (1981) that the $x(p)$ data carry more information about the gradients at the turning depths, and the $\tau(p)$ data more about absolute velocity at a given depth. The scatter in the higher velocity regions is primarily due to incomplete editing of near surface multiple peaks from the data. Although it was a little hard to see on the image, the agreement of the predictions of deeper regions of the model with the observed offset data is good. This is seen more readily in Fig. 21. In this plot, both the $x(p)$ and $\tau(p)$ data and predictions from the model in Fig. 20 are shown.

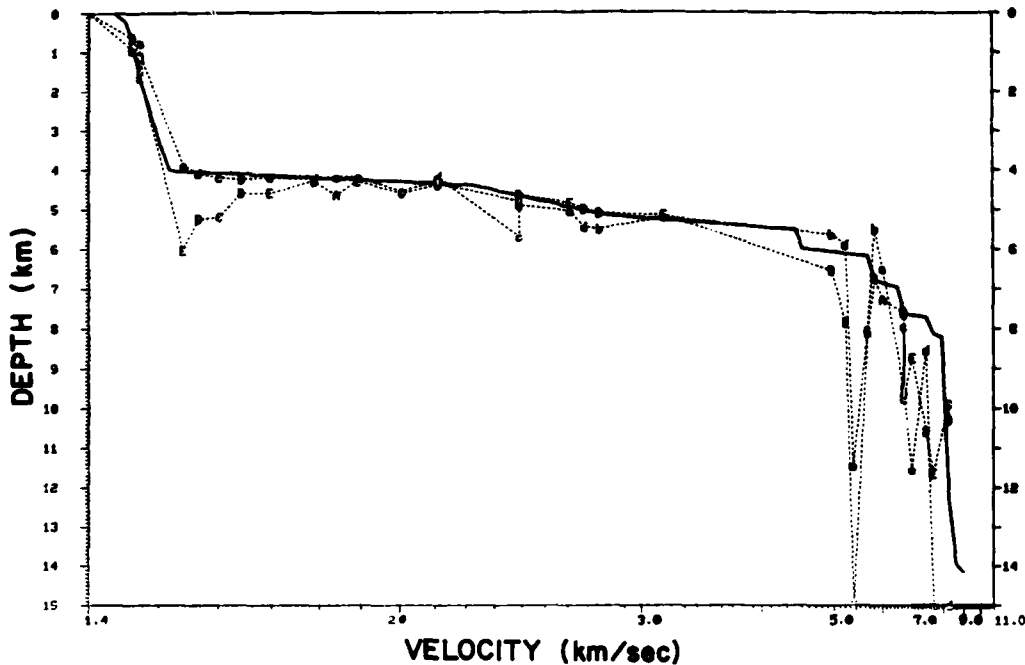


Fig. 20. Trial compressional model and migrated data image for 14 Hz data from all six shots and multiples. The heavy solid curve is the trial model, the dotted curve with lower case labels is the τ data image, and the dotted curve with the upper case labels is the offset image.

Figure 22 shows a trial model (solid line) and the imaged τ (lower case letters and dotted line) and x (upper case letters and dotted line) data for the shear conversions at the basement. The agreement is quite good, except just at the base of the water column, which indicates the need for a decreased gradient. The data and predicted curves are given in Fig. 23. The offset matching by this model is seen to be very good.

Summary for line 1

The results of refraction line 1 indicate a crust that is slightly thinner than average oceanic crust (Christensen and Salisbury, 1975) in this region of slow crustal spreading (0.5 cm/yr). The high gradient sediments cover a smooth basement, and the strong shear conversions indicate a high-velocity contrast with the base of the sediments. Using the assumptions of Baggeroer and Falconer (1982) and a depth to basement (defined by 5 km/s compressional sound speed) of 2.1 km, the result of calculating the unloaded depth to basement yields an estimate of crustal age using the relationship of Parsons and Sclater (1977) which is in agreement with the interpretation of the magnetic anomaly pattern (Vogt et al., 1979). Both of these techniques estimate the age of the crust for this line at around 50 Ma (late Eocene).

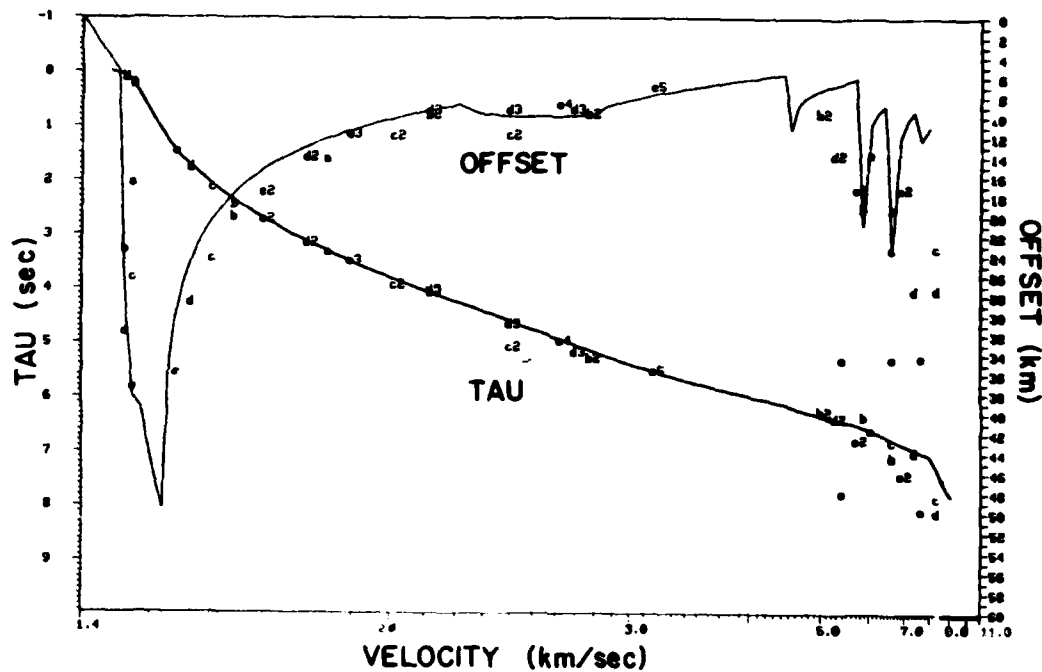


Fig. 21. The 14 Hz peak $\tau(p)$ and $x(p)$ data (letters) and the curves predicted by the model of Fig. 20.

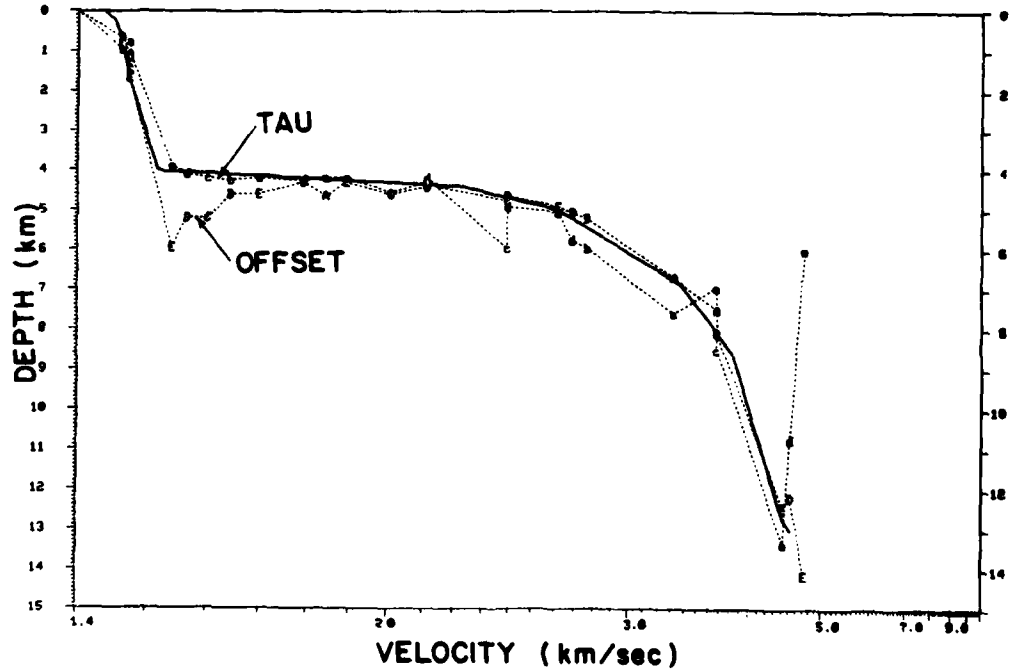


Fig. 22. Trial shear wave model and data image for 14 Hz data from all six shots and multiples. The heavy solid curve is the trial model, the dotted curve with lower case labels is the τ data image, and the dotted curve with the upper case labels is the offset image.

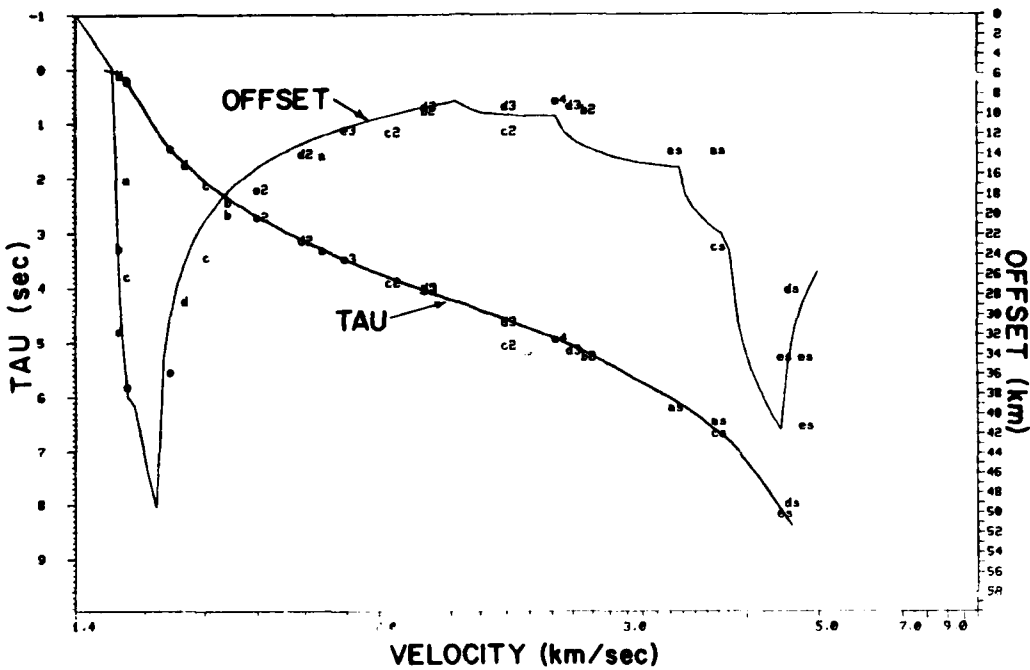


Fig. 23. The 14 Hz peak $\tau(p)$ and $\chi(p)$ data (letters) and the curves predicted by the shear wave model of Fig. 22.

The estimated offset function from this line also gives evidence of a variable gradient structure in the deep layer 2 and layer 3-Moho region.

Fram 2 line 4

Experimental parameters

Refraction line 4 began on April 21, 1980. For the initial shot at 1900 Z the Fram 2 camp was located at 86.10°N and 24.78°W . At the end of shooting on the 21st at 2030Z (33.45 km offset) the camp had moved negligibly. The second day of shooting for this line was April 22, and began at 1500Z at an offset of 43.2 km. The initial location of the camp was 86.07°N and 24.87°W . This is 4.3 km south of the previous day's shooting. The final shot of this line was dropped at 2000Z when the receiving array was at 86.053°N and 24.876°W . The drift was still southerly, and this location is 1.3 km south of the initial shot on this day, and 5.6 km south of the previous day's shooting.

For this line, water-wave traveltimes were accurate and the shot offsets well determined. The parameters for the shots in line 4 are summarized in Table 4. At this time the entire 24 channel array was deployed; however, three channels were omitted from the data processing either because of connection

TABLE 4

Shot parameters for Fram 2 line 4

Charge weight (kg)	Depth @ rcvr (km)	Depth @ src (km)	Dip (deg.)	Range (km)	Bearing (true deg.)
25	3.805	3.85	0.20	13.25	91.5
25	3.805	3.85	0.17	16.91	89
25	3.805	3.88	0.17	25.67	93
25	3.805	3.91	0.21	28.14	92
25	3.805	3.96	0.26	33.45	92
50	3.806	3.99	0.24	43.23	93
50	3.807	4.00	0.24	45.79	94
50	3.807	4.03	0.24	52.70	95
50	3.807	4.05	0.24	57.25	95
50	3.807	4.08	0.24	63.04	91
100	3.808	4.10	0.23	71.82	92
100	3.808	4.15	0.22	87.88	93

problems or because they were used for recording other instruments. These locations are slightly different from line 1 because part of the array broke away due to ice movement on April 16, 1980.

Discussion

Line 4 is in a region 200 m shallower than line 1 and runs almost orthogonal to it. The overall location is south of line 1, closer to the Morris Jessup Rise. Since this line heads east from the camp, perpendicular to the isochrons, it is expected that the structure will adhere less to laterally homogeneous assumptions than line 1. In addition, the camp movement between halves of the line leads to additional scatter in the data. The receiving array was located at magnetic anomaly 23. Anomaly 22 was at a range of 16 km, anomaly 21 at 43 km, and anomaly 20 at 77 km to the east. The bathymetry decreased toward the receivers with a dip of 0.25° , thus possibly biasing the measured phase velocities upward. Apart from differences in the crustal structure, we would expect that because of the shallower water depth, the τ values will be 0.2–0.3 s less than those of line 1.

To predict what to expect from line 4, we compare some of the features of a velocity spectrum from line 4 to one of line 1 with a similar offset. This expedites comparison, and we will note some qualitative features. The major difference between an offset of 13.25 km on line 4 (Fig. 24a *) and 13.4 km on line 1 (Fig. 24b)

* The numbers on the plots 24a, b are the local maxima picks of the peak picking algorithm before editing out the unimportant detections. These should be ignored.

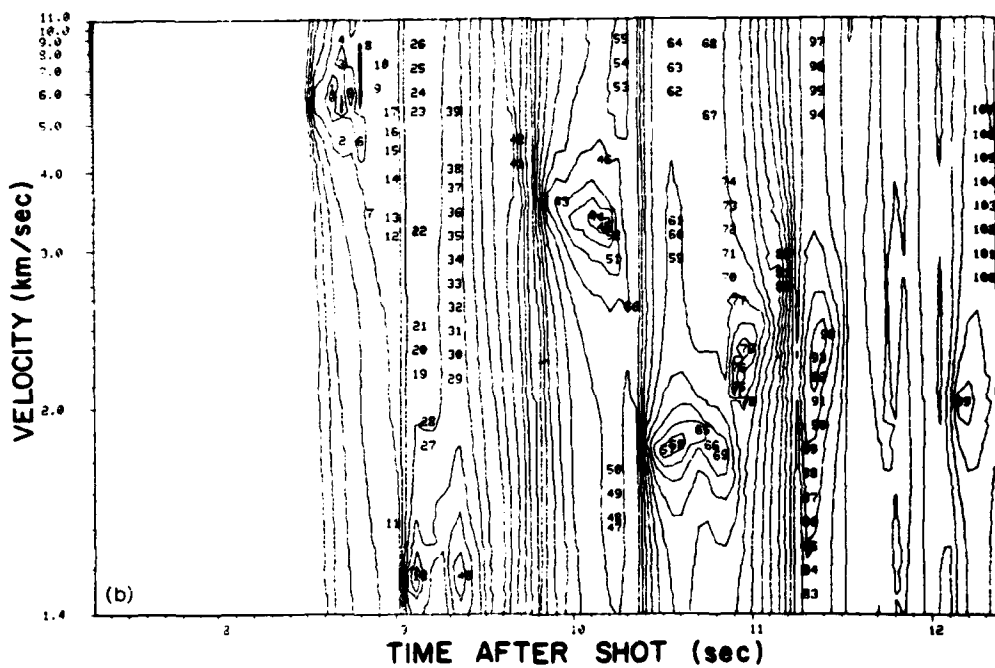
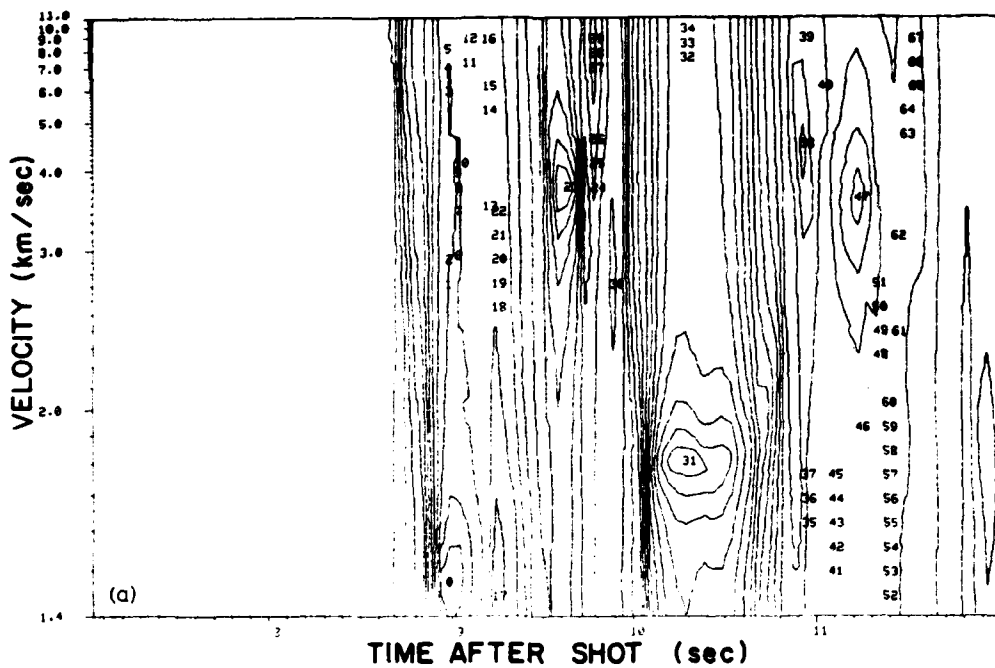


Fig. 24. a. The 6 Hz velocity spectrum for Fram 2 line 4 at an offset of 13.25 km. The contour intervals are 5.0 dB. b. The 6 Hz velocity spectrum for Fram 2 line 1 at an offset of 13.4 km. The contour intervals are 5.0 dB.

is that the deep arrival at 5.8–6.0 km/s which has broken out in front of the direct water arrival on line 1 has not yet appeared on line 4 (it is probably lost in the water wave side lobe artifact). This indicates that despite the shallower water, there is a larger delay time, τ , at a given slowness for line 4, indicating a thickening of the sedimentary layers or upper igneous crust. Adhering to isostatic gravity arguments, the bathymetric shoaling would also support this interpretation.

The similarities of the rest of the sections are high, and a high gradient is expected in the sediments because of the near-surface multiple characteristics. The arrivals from line 4 (Fig. 24a) and line 1 (Fig. 24b) at 9.6 and 9.9 s, and 3.8 and 3.5 km/s which have been identified as having been converted to shear at the basement interface also show a 0.2 s larger τ for the line 4 events. The velocity spectra for other offsets of line 4 are similar to those of nearby offsets on the line 1, although there is significantly more multipath on line 4, a result, perhaps, of greater lateral heterogeneity.

The initial inversions using the velocity–depth migration algorithm on peak picked data support the qualitative features mentioned above. Although the Moho is also poorly constrained on this line, the τ values for layers 2 and 3 are larger on line 4 than line 1, leading to a model with a thicker sedimentary section, as shown in Fig. 25.

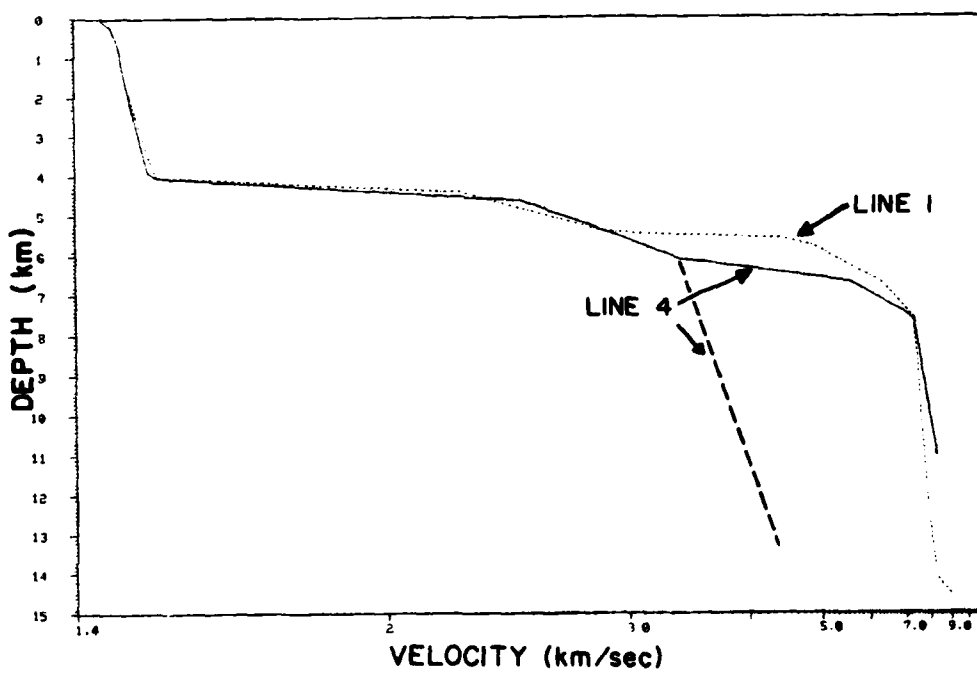


Fig. 25. The shear model for line 4 (dashed) and the compressional models for line 1 (dotted) and line 4 (solid).

As with the compressional data, the shear arrivals show significant scatter. The shear conversions are again at the basement interface as in line 1. The observed shear data indicate a larger depth to lower layer 3 and mantle velocities than the compressional data. This discrepancy cannot be reconciled due to the large scatter in the traveltimes and offsets measured for the deeper data. The models are compared with the line 1 compressional model in Fig. 25.

A reduced traveltimes vs. offset display of the line 4 data and model predictions is shown in Fig. 26. The data are indicated by the letters on the plot after datum correction and reduction of the free surface multiples to the primary curve. The $x-t$ curve of the line 4 compressional model in Fig. 25 is shown by the solid line. The first arrivals are well modeled according to this plot. An interesting feature of the data is the long string of arrival peaks at an offset of 16.9 km. The later components of this series are in a position to result from shadow zone arrivals from the triplication cusp reaching out to 11 km. The earlier arrivals would also be better predicted if the model had included some gradient changes in layer 3. The arrivals in this complex are quite energetic, and the 6 Hz, 16.9 km velocity spectrum from which the arrivals were picked is shown in Fig. 27. The heavy solid line is the Θ function defined by Chapman (1978). This was computed using the compressional

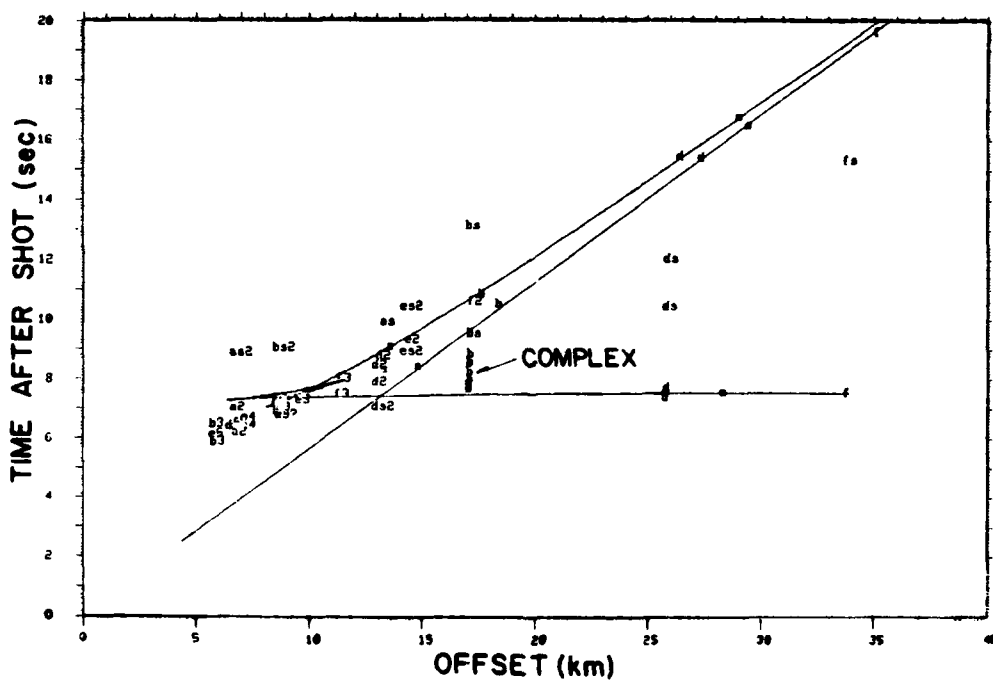


Fig. 26. Datum corrected and free surface "condensed" data for 6 Hz band on line 1 (letters). A number appearing in the labels indicates the suspected free surface multiplicity. An "s" in the label indicates a suspected shear path. The plot is reduced on 8 km/s.

model of Fig. 25 and the experimental source and receiver depths. The non-infinite slope of the line shows that the arrivals at 4–6 km/s after the first at about 7.3 km/s are not geometrical for the model used. However, a model close to the model used, but with more definite layering would have larger cusps, and would have more "ripples" in the Θ function in the area between 4 and 6 km/s, thus leading to prediction of significant amplitudes in this region. This supports the indications noted in the discussion of line 1 that there could be significant gradient changes in the layer 2 and layer 3 regions.

Fram 2 line 6

Experimental parameters

This short 5-shot line was carried out on April 18, 1980. The first shot, at 1400Z, was initiated when the camp was located at 85.77°N and 24.24°W as the bathymetry beneath the camp began to shoal on the approach to the Morris Jessup Rise. The line was completed by 1530Z and camp movement was negligible during this period. For this line all systems were operating well, and the parameters for the shots are

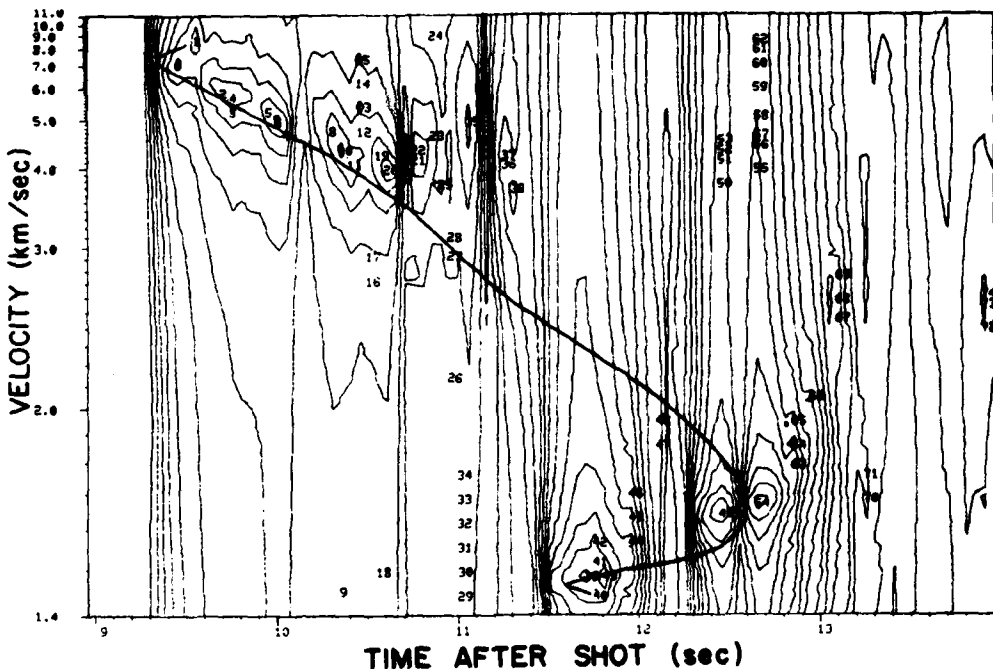


Fig. 27. Velocity spectrum at 6 Hz for Fram 4 line 4 at an offset of 16.9 km (contours). The Θ function defined by Chapman (1978) is plotted by the heavy solid line for the primary arrival with no free surface interactions. This was computed using the line 4 compressional model of Fig. 25 and the experimental source and receiver depths.

tabulated in Table 5. The array locations were nearly the same as those for line 4, although one more sensor had been activated.

Discussion

Line 6 is similar to line 4 in that the shots were deployed over crust with decreasing age as the offset increased. This line covered a region with a significant dip of about 0.6° , with depth increasing with offset. If this region were one of normal oceanic crust, the decreasing bathymetry on this line and an isostatic gravity compensation assumption would lead to the conclusion that the Moho would be depressed, igneous crustal thickness would be constant, and thicker sediments would be found in this region than deeper in the Pole Abyssal Plain. However, the Morris Jessup Rise on which this line shoaled is hypothesized to be a region of thickened oceanic crust which formed at the Arctic Mid-Ocean Ridge at anomaly 18-13 time, along with the Yermak Plateau (Feden et al., 1979). One of the major arguments for this is that plate reconstructions for this time require that the Morris Jessup Rise and the Yermak Plateau be oceanic to avoid continental overlap (e.g., Jackson et al., 1984). Another piece of corroborative evidence for crustal thickening is the "magnetic high" (Vogt et al., 1979; Feden et al., 1979) observed in the magnetic anomaly over the Rise. This could be due to increased magnetization, but may also indicate increased layer 2 thickness.

Ostenso and Wold (1977) ran a single channel seismic reflection profile across the Morris Jessup Rise during the ARLIS 2 experiment (1964). Their stations numbered 63-65 were close (30 km distant) to the area surveyed by line 6. The penetration of the single channel system was only about 0.5 s (two-way traveltime) and basement is not defined in our area. They concluded that the sediment was generally thick in this region, but the paucity and quality of the data makes the seismic results somewhat inconclusive. In addition, their data does not cover the line 6 location. These points are raised, of course, because our refraction data indicate a somewhat different structure for the sediments on this line.

The $\tau(p)$ and $x(p)$ data for line 6 at all frequencies are composited and

TABLE 5
Shot parameters for Fram 2 line 6

Charge weight (kg)	Depth @ rcvr (km)	Depth @ src (km)	Dip (deg.)	Range (km)	Bearing (true deg.)
25	3.655	3.75	0.55	9.45	104
25	3.655	3.85	0.77	14.18	100
25	3.655	3.89	0.74	18.28	98
25	3.655	3.90	0.65	21.64	97
25	3.655	3.90	0.59	23.37	97

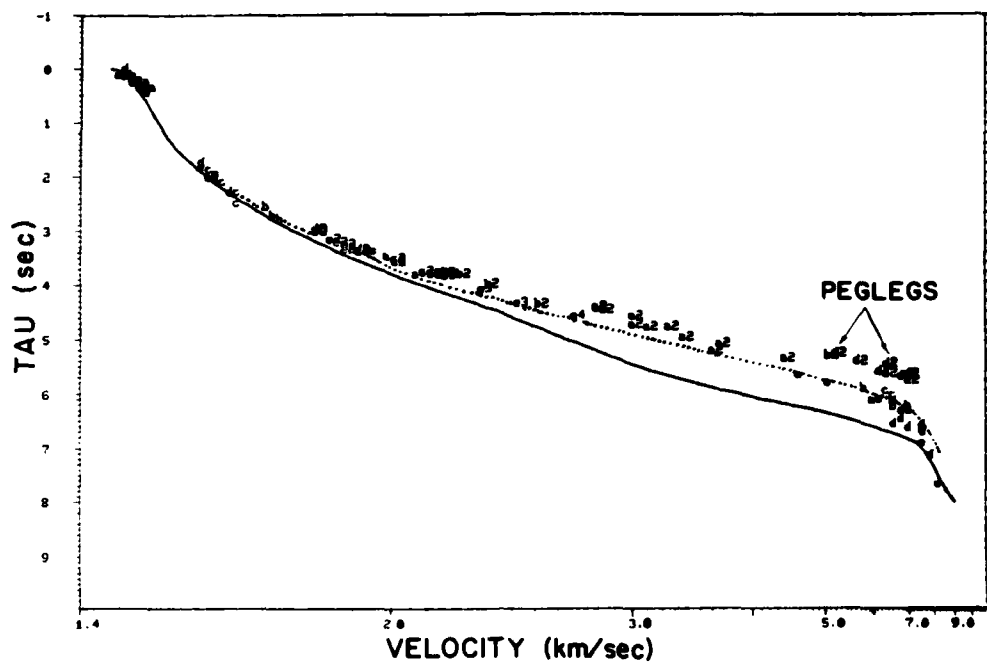


Fig. 28. The condensed and corrected $\tau(p)$ data (letters) and the $\tau(p)$ curve generated by the model of Fig. 29 for line 6 (dotted). The $\tau(p)$ curve representative of the data from line 1 is given by the solid line.

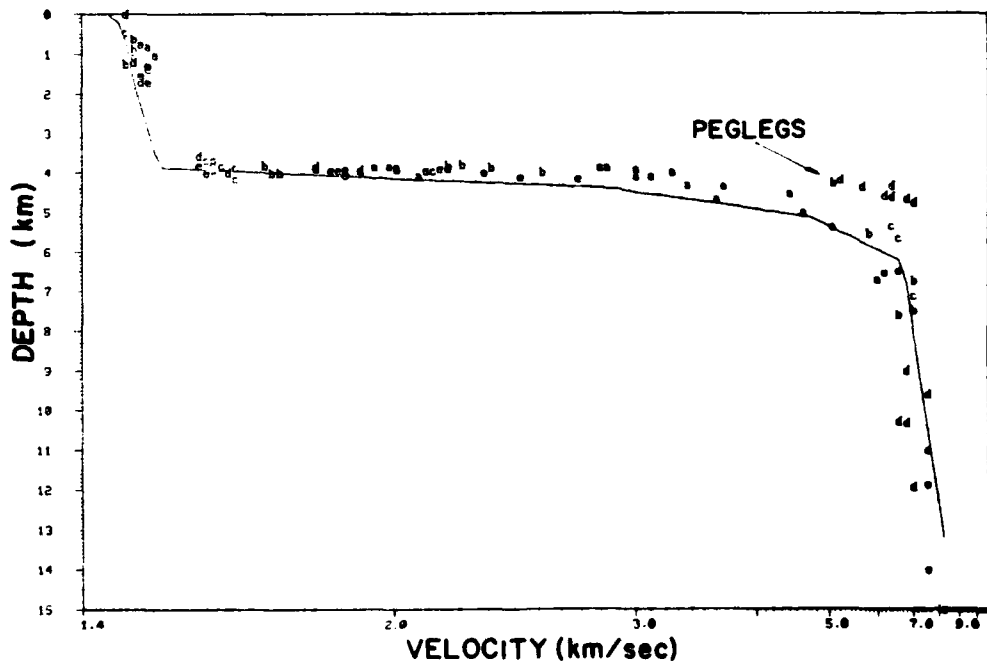


Fig. 29. The compressional velocity-depth migration results for Fram 4 line 6.

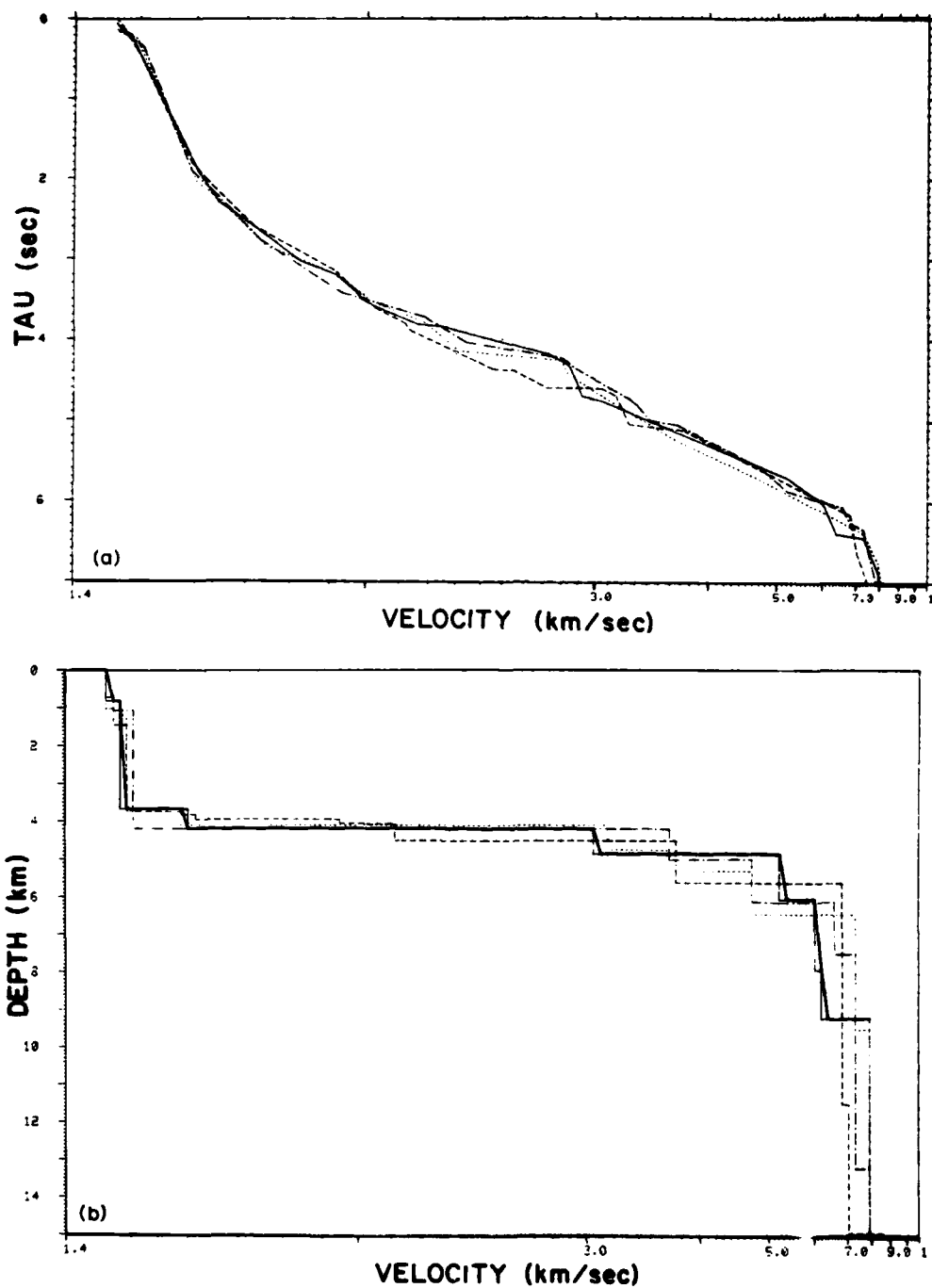


Fig. 30. a. The $\tau(p)$ curves linearly interpolating the picked peaks for line 6 at the four different velocity spectral analysis frequencies. b. The models resulting from inversion of the picked peaks used to construct the $\tau(p)$ curves in Fig. 30a by the τ -sum method.

condensed in Fig. 28 after correction to the surface datum and correction of the observed phase velocities for the 0.6° bathymetric dip. Note that the scatter on this line is very low. The $\tau(p)$ curve from line 1 superposed on this plot shows that the water column is thinner (the decreased τ for most regions of the curve for line 6) but that the total depth to Moho must be somewhat larger than that of line 1 due to the matching of the τ values at velocities of 7.4–8 km/s. Since this profile has lost 350 m of very slow water column, the crust and sediments must thicken noticeably, or have a larger region of lower velocity strata, or both, to retain this feature. The presence of the water column pegleg arrivals (noted on the plot) indicates that the top of the sediments is highly consolidated. This agrees with the turbidite sediment constitution hypothesis of Ostenso and Wold (1977).

The results of velocity-depth migration on these data are shown in Fig. 29. In this figure the migrated data and trial model are shown by the letters and solid line, respectively. The pegleg data at layer 2/layer 3 velocities have been ignored, as have some of the early arriving multiples in the sedimentary velocity region. This is because it is felt that a significant portion of the early arriving energy is due to water column pre-critical peglegs, although the differences in τ for the shallower events do not allow good separation of the direct and true free surface multiples from the pegleg paths. The data and predicted $\tau(p)$ curve are compared for this model in Fig. 28. Note that the suspected pre-critical arrivals proceed horizontally from the $\tau(p)$ curve as discussed by Clayton and McMechan (1981).

The τ -sum method for homogeneous layers was also used on the $\tau(p)$ data in Fig. 30a. The lower dashed curve is the lowest frequency (8 Hz) and is the least influenced by the pre-critical reflections which we hypothesize to cause the bulge between 2 and 3 km/s. The higher velocity peglegs mentioned earlier are not included in these curves. The results of the τ -sum inversions are in Fig. 30b. These are in good agreement with the migration result of Fig. 29. The envelope of the curves is indicative of the uncertainty in the resulting model. In general, the models indicate a slightly shallower depth to basement than is correct because of the use of the precritical reflection peglegs. However, these arrivals tend to make infeasible models when inverted by the τ -sum method, and were eliminated by a modification to the τ -sum recursion (Duckworth, 1983).

The results for line 6 indicate a thinner sedimentary region than that observed on lines 1 and 4. They also indicate a thicker igneous crust, agreeing with current hypotheses that attribute a thickened oceanic crustal structure to the Morris Jessup Rise. Another line which has not yet been interpreted (Fram 2, line 5, see Fig. 1) samples the rise much more extensively and should confirm the data reported here. The only anomalous result for this line is the lack of a thick sedimentary cover.

THE FRAM 4 EXPERIMENT IN THE NANSEN BASIN

The Fram 4 experiment was carried out in March–May of 1982 in the Nansen Basin of the Eastern Arctic Ocean. This experiment was very similar to the Fram 2

effort; refraction shots were deployed by helicopter and received by a 24 channel 2-D hydrophone array suspended beneath the ice. Processing and inversion techniques were identical to those used on the Fram 2 data. The Fram 4 camp and array layout are given in Fig. 31.

Fram 4 (see Fig. 1) was on the eastern side of the Arctic Mid-Ocean Ridge near the Yermak Plateau and above anomaly 12. This is on younger crust than that covered by the Fram 2 experiment. Figure 3 shows the drift track and the refraction lines carried out during this experiment. This paper will deal only with lines 1 and 4, and the analysis of these lines is somewhat preliminary. For this experiment, the refraction lines were shot along one azimuth to enable reception on a linear hydrophone array deployed by other investigators (Kristoffersen and Husebye, 1985, this volume). The small deviations in azimuth from one line to another are due to the rotation of the ice pack changing the orientation of this array.

A summary of the morphology of the Yermak Plateau is given by Sundvor et al. (1982). Plate reconstructions (Feden et al., 1979; Jackson, 1985; Srivastava, 1985) indicate that the Yermak Plateau must be composed of oceanic crust to avoid

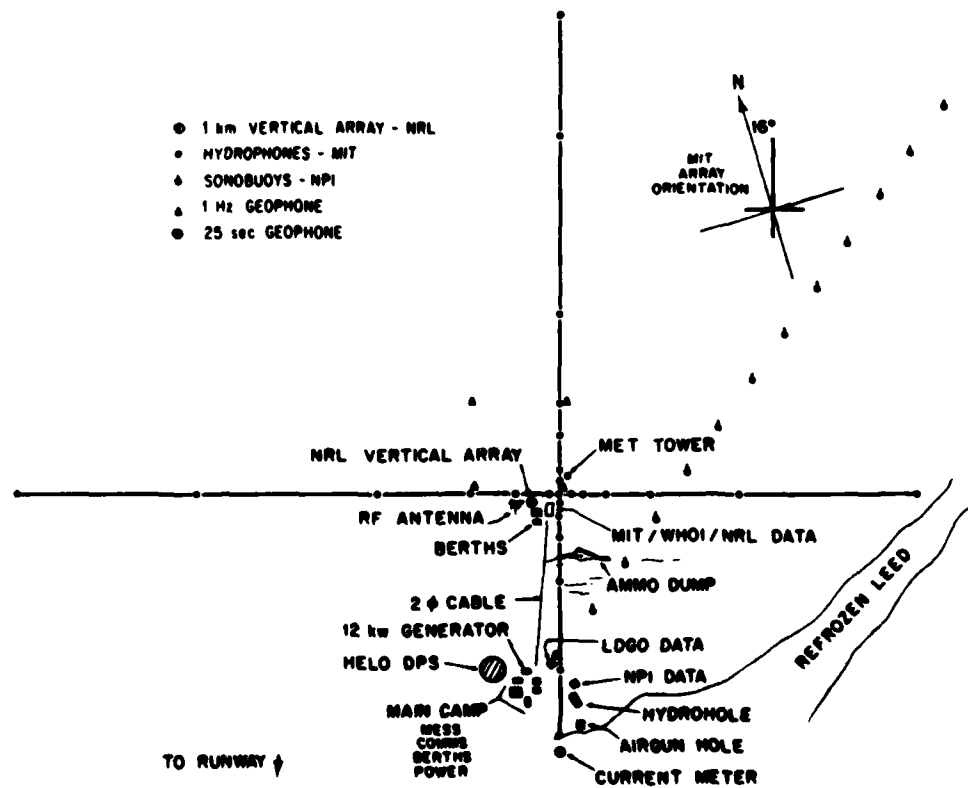


Fig. 31. The Fram 4 ice camp, showing the locations of the horizontal hydrophone array elements and the camp buildings.

overlap between Greenland and the Eurasian Plate at Svalbard in the early Tertiary period. Feden et al. (1979) suggest that the Yermak Plateau and Morris Jessup Rise were formed from a hot-spot at the spreading center of the Arctic Mid-Ocean Ridge at anomaly 13-18 time. This hotspot has since dissipated, and the two features separated through sea-floor spreading.

Fram 4 line 1

Line 1 was carried out on April 1, 1982 (Day 91). At the start of the refraction run (1020 Z) the camp was at 83.87°N, 19.33°E. At the end of the run (1730 Z), the camp position was 83.86°N, 19.33°E, 1.2 km from the position at 1020 Z. The shot parameters are summarized in Table 6.

Because the techniques used for the Fram 4 analysis are similar to those used for the previously discussed Fram 2 data, this section will be brief, and the preliminary model results will be emphasized. Figure 32 plots the picked, corrected, and multiple condensed $\tau(p)$ and $x(p)$ data at 14 Hz for line 1. Note that in contrast with the Fram 2 results, these data do not indicate strong shear wave arrivals. The offset data again hint that there may be significant gradient changes in lower layer 2 and layer 3. The solid lines on the plot indicate the τ and offset curves for a model determined by velocity/depth migration using hand picking of the trial models at each step. This method was used to eliminate arrivals which were known to be precritical or near-surface multiples, and to interpolate the model with the desired prejudices in

TABLE 6
Shot parameters for Fram 4 line 1

Charge weight (kg)	Depth @ rcvr (km)	Depth @ src (km)	Dip (deg.)	Range (km)	Bearing (true deg.)
25	3.98	3.98	0	9.44	209
25	3.98	3.98	0	17.84	213
25	3.98	3.98	0	19.52	210
25	3.98	3.99	0	21.53	212
25	3.98	3.97	0	25.35	212
25	3.98	3.97	0	29.34	212
50	3.98		0	32.54	212
50	3.98		0	40.47	213
50	3.98		0	44.32	212
50	3.98	3.98	0	41.68	214
50	3.98	3.98	0	50.60	213
50	3.98	3.98	0	56.14	214
50	3.98	3.98	0	60.73	215
100	3.98	3.97	0	69.32	212

regions of sparse sampling. The model for the compressional profile is given in Fig. 34. The traveltimes vs offset data and predictions for this model are given in Fig. 33. It can be seen from this display that the sediment multiples are well predicted, and that the crossover distance to upper mantle refractions is quite small—approximately 17 km, indicating a thin crust.

The sediment thickness for this line is estimated to be 1.6–1.7 km thick, giving a crustal age estimate of 41.5–43 Ma using the relationship of Parsons and Sclater (1977) and the assumptions of Baggeroer and Falconer (1982). This exceeds the late Oligocene age of approximately 35 Ma associated with anomaly 12, and agrees with the findings of thick sediments reported by Kristoffersen and Husebye (1985, this volume).

Fram 4 line 4

The position of the camp at the beginning of line 4 at 1720 Z, April 19, 1982 (day 109) was 83.43°N, 14.71°E. At the end of the first day's run at 2300 Z, the camp position was 83.41°N, 14.70°E, 1.7 km from the starting location. When the shooting resumed on April 20, 1982 (Day 110) at 1000 Z, the camp position was 83.39°N and 14.71°E. This is 2.4 km from the previous day's end point. The line

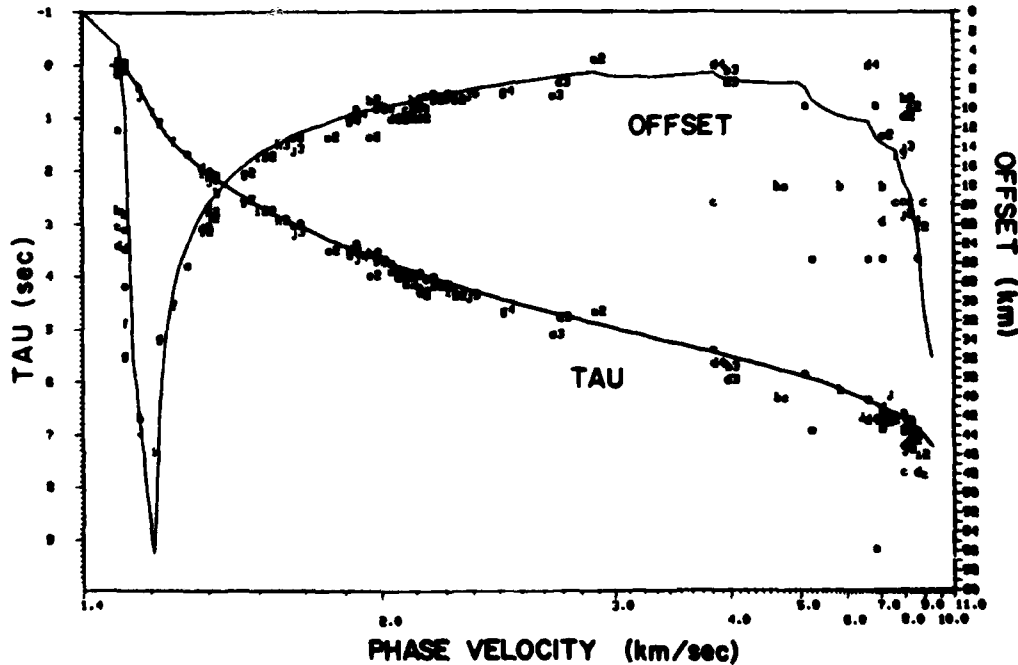


Fig. 32. The $\tau(p)$ and $x(p)$ data from Fram 4 refraction line 1. These data points were picked from the 14 Hz velocity spectra.

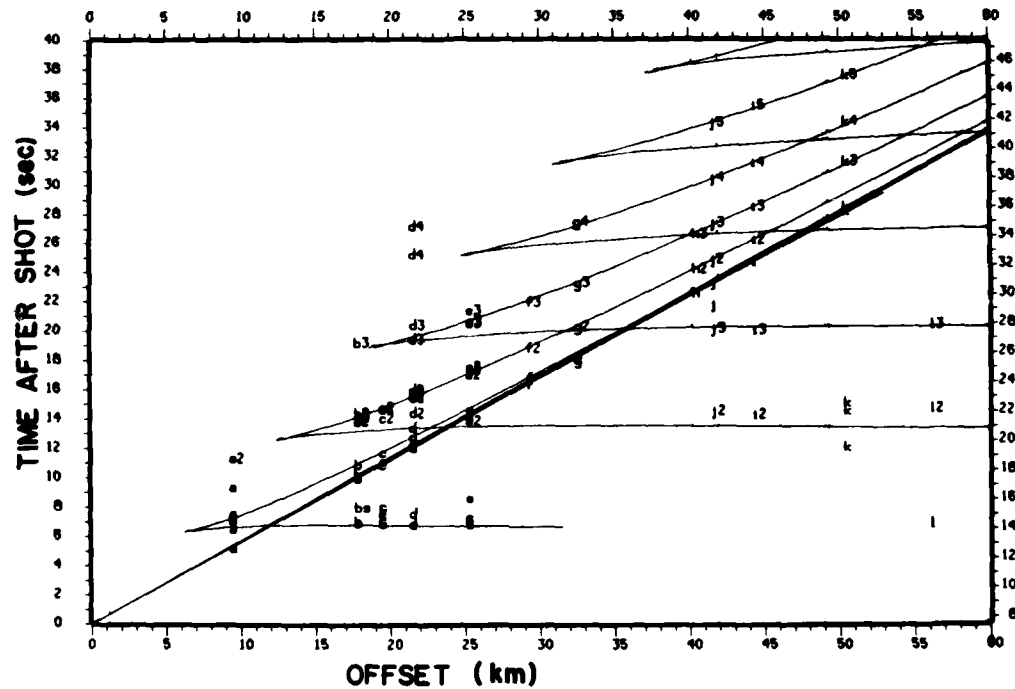


Fig. 33. The traveltimes data from Fram 4 line 1 picked from the 14 Hz velocity spectra (letters and number labels). The predicted traveltimes curves from the Fram 4 line 1 compressional model of Fig. 34 are given by the solid lines for the first 5 multiples.

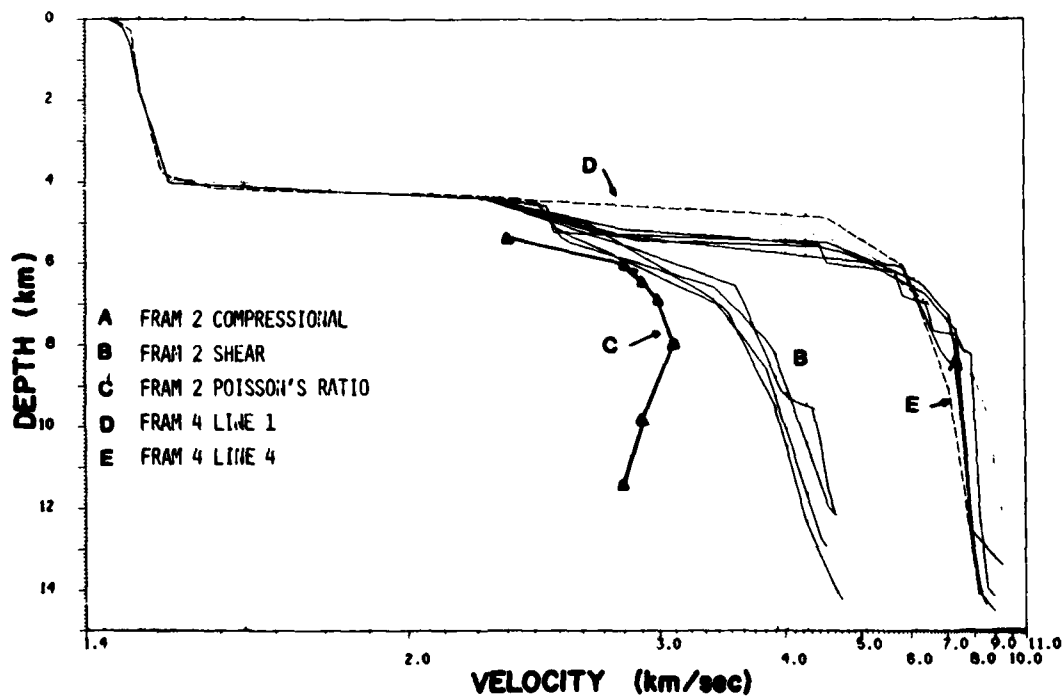


Fig. 34. Comparison of the velocity/depth models for Fram 2 line 1 and Fram 4 lines 1 and 4.

TABLE 7

Shot parameters for Fram 4 line 4

Charge weight (kg)	Depth @ revr (km)	Depth @ src (km)	Dip (deg.)	Range (km)	Bearing (true deg.)
25	3.99	3.97	-0.1	10.61	198
25	3.99	3.89	-0.33	17.45	198
25	3.99	3.88	-0.32	20.00	200
25	3.99	3.79	-0.5	23.27	200
25	4.00	3.96	-0.1	26.81	201
25	3.99	3.96	-0.1	29.28	205
25	3.99	3.97	0	33.72	205
25	3.99	3.97	0	37.85	205
50	3.99	3.97	0	40.77	203
50	3.99	3.97	0	39.30	203
50	3.99	3.97	0	46.25	206
50	3.99	3.98	0	53.09	207
50	3.99	3.97	0	58.63	207

finished only an hour later with negligible change in position. Table 7 contains the shot parameters for this line.

Line 4, closer to the Yermak Plateau than line 1, showed a similar lack of clearly identifiable shear path arrivals. Much more detailed analysis is now being carried out on these data, but preliminary inversions using the velocity-depth migration technique indicate that the depth to Moho is greater for this line than Fram 4 line 1, or the lines discussed earlier from Fram 2. A representative model is shown in Fig. 34. This figure also indicates the results from Fram 2 line 1 for the compressional velocity, shear velocity, and Poisson's ratio for comparison.

The sediment thickness of 1.4–1.5 km determined on this line leads to an estimated crustal age of 38–40 Ma using the assumptions stated earlier, and is again in excess of the expected thickness for the magnetic anomaly 12 dating of 35 Ma (Vogt et al., 1979).

SUMMARY

In this paper we have shown that the use of horizontal two-dimensional arrays in the central Arctic pack ice can provide refraction data that may be inverted by current traveltime inversion methods. The use of advanced signal processing algorithms allowed the estimation of well sampled $\tau(p)$ and $x(p)$ curves with a minimum number of shots through the use of all free surface multiples. Examples were given to show how such data may be inverted by τ -sum, velocity/depth migration, and extremal techniques.

The results of the crustal structure estimates indicate that the crustal thicknesses in the abyssal plain regions on either side of the spreading center at the Arctic Mid-Ocean Ridge are slightly thinner than average. The Fram 2 experiment near the Morris Jessup Rise indicated a thickened, but continued oceanic crustal structure as the rise was approached. The sediment thickness in the region generally agrees with that expected from its age as obtained from magnetic anomaly dating, however, the line highest on the flank of the Morris Jessup Rise indicates an anomalously thin sediment structure. The line deepest in the abyssal plain showed extremely good conversions from compressional to shear wave energy which may indicate a very smooth basement structure. The strong shear arrivals also allow good estimates of the Poisson's ratio in layer 2 and layer 3.

The Fram 4 lines indicate a much rougher basement topography, with no shear arrivals being unequivocally detected to date. The sediment structure is thicker than expected for the late Oligocene crustal age predicted by the magnetics, and may be a reflection of the location of the experiment in a region which may have sediments deposited after transport by the Transpolar Drift.

ACKNOWLEDGEMENTS

The acquisition of refraction data in an environment such as the Arctic ice pack requires the cooperation of a large number of people to be safe and productive. The authors wish to thank their colleagues at the Woods Hole Oceanographic Institution, especially Keith von der Heydt and David Gever, for their development and support of the hardware and software necessary for the acquisition and processing of these data. The logistical support and environmental data acquisition provided by the University of Washington's Polar Science Center and the Lamont-Doherty Geological Observatory was also essential. We are also grateful for our many discussions with Ruth Jackson of the Bedford Institute of Oceanography, and thank Shane Ingate for his helpful comments on the final manuscript.

This work was supported by the Office of Naval Research, Arctic Programs Office, through contracts N 00014-77-C-0266 at MIT, and N 00014-80-C-0161 through N 00014-84-C-0161 at WHOI.

REFERENCES

Allen, B., Arda, J., Hunkins, K., Lee, T., Manley, T.O. and Tiemann, W., 1980. Observations of position, ocean depths, and gravity taken from the Fram II and Camp I drifting ice stations. *Lamont-Doherty Geol. Obs. Tech. Rep.*, CU-13-80.

Baggeroer, A.B. and Falconer, R.K.H., 1982. Array refraction profiles and crustal models of the Canada Basin. *J. Geophys. Res.*, 87: 5461-5476.

Bessonova, E.N., Fishman, V.M., Ryaboyi, V.Z. and Setnikova, G.A., 1974. The tau method of inversion of travel times. I. Deep sounding seismic data. *Geophys. J. R. Astron. Soc.*, 36: 377-398.

Bott, M.H.P., 1982. *The Interior of the Earth: Its Structure, Constitution, and Evolution*. Arnold, London, 2nd ed., 403 pp.

Capon, J., Greenfield, R.J. and Kolker, R.J., 1967. Multi-dimensional maximum likelihood processing of a large aperture seismic array. *Proc. I.E.E.E.*, 55(2).

Chapman, C.H., 1978. A new method for computing synthetic seismograms. *Geophys. J. R. Astron. Soc.*, 54: 481-518.

Christensen, N.I. and Salisbury, M.H., 1975. Structure and constitution of the lower oceanic crust. *Rev. Geophys. Space Phys.*, 13(1): 57-86.

Clayton, R. and McMechan, G., 1981. Inversion of refraction data by wavefield continuation. *Geophysics*, 46(6): 860.

Diebold, J.B. and Stoffa, P.L., 1981. The travelttime equation, tau-p mapping, and inversion of common midpoint data. *Geophysics*, 46(3): 238-254.

Dorman, L. and Jacobson, R.S., 1981. Linear inversion of body wave data. Part I. Velocity structure from travel times and ranges. *Geophysics*, 46(2): 138-151.

Duckworth, G.L., 1983. Processing and inversion of Arctic Ocean refraction data. Sc. D. Thesis, Mass. Inst. Technol.; Dep. Electr. Eng. Comput. Sci. and Woods Hole Oceanogr. Inst.; Dep. Oceanogr. Eng.

Duckworth, G.L., Baggeroer, A.B. and Jackson, H.R., 1982. Crustal structure measurements near FRAM II in the Pole abyssal plain. *Tectonophysics*, 89: 172-215.

Feden, R.H., Vogt, P.R. and Fleming, H.S., 1979. Magnetic and bathymetric evidence for the Yermak hot spot northwest of Svalbard in the Arctic Basin. *Earth Planet. Sci. Lett.*, 44: 18-38.

Jackson, H.R., 1985. Nares Strait—A suture zone: geophysical and geological implications. *Tectonophysics*, 114 (this issue): 11-28.

Jackson, H.R., Reid, I. and Falconer, R.K.H., 1982. Crustal structure near the Arctic Mid-ocean Ridge. *J. Geophys. Res.*, 87(B3): 1773-1783.

Jackson, H.R., Johnson, G.L., Sundvor, E. and Myhre, A.K., 1984. The Yermak Plateau: formed at a triple junction. *J. Geophys. Res.*, 89 (B5): 3223-3232.

Kristoffersen, Y. and Husebye, E.S., 1985. Multichannel seismic reflection measurements in the Eurasian Basin, Arctic Ocean, from U.S. Ice Station Fram IV. *Tectonophysics*, 114 (this issue): 103-115.

Ness, G., Levi, S. and Couch, R., 1980. Marine magnetic anomaly timescales for the Cenozoic and late Cretaceous: a précis, critique, and synthesis. *Rev. Geophys. Space Phys.*, 18: 753-770.

Ostenso, N.A. and Wold, R.J., 1977. A seismic and gravity profile across the Arctic Ocean Basin. *Tectonophysics*, 37: 1-24.

Parsons, B. and Sclater, J.G., 1977. An analysis of the variation of ocean floor bathymetry and heat flow with age. *J. Geophys. Res.*, 82: 803-827.

Spudich, P. and Orcutt, J., 1980. A new look at the seismic velocity structure of oceanic crust. *Rev. Geophys. Space Phys.*, 18: 627-645.

Srivastava, S.P., 1985. Evolution of the Eurasian Basin and its implication to the motion of Greenland along Nares Strait. *Tectonophysics*, 114 (this issue): 29-53.

Sundvor, E., Johnson, G.L. and Myhre, A., 1982. Some aspects of morphology and structure of the Yermak Plateau NW of Spitsbergen. *Seismol. Obs. Univ. Bergen, Sci. Rep.*, 8.

Tiemann, W., Arda, J., Allen, B. and Manley, T.O., 1982. Geophysical data from drifting ice stations Fram IV and Tristen, Lamont-Doherty Geol. Obs., Palisades, N.Y. Tech. Rep. LDGO-82-3.

Vogt, P.R., Taylor, P.T., Kovacs, L.C. and Johnson, G.L., 1979. Detailed aeromagnetic investigations of the Arctic basin. *J. Geophys. Res.*, 84: 1071-1089.

Weston, D.E., 1960. Underwater explosions as acoustic sources. *Proc. Phys. Soc.*, 76: 233.